Finanziato dall'Unione europea NextGenerationEU | Ministero dell'Università e della Ricerca | Italiadomani PIANO NAZIONALE DI RIPRESA E RESILIENZA

multi-Risk sciEnce for resilienT commUnities undeR a changiNgclimate

Codice progetto MUR: **PE00000005** – F83C22001660002

Deliverable title: Improved methodologies for contaminant monitoring

Deliverable ID: DV 4.3.1

Due date: February 29th, 2024

Submission date: February 29th, 2024

AUTHORS

Manuela Antonelli, Beatrice Cantoni, Chiara Recalcati, Laura Ceresa, Alberto Guadagnini, Enrico Zio, Davide Marzi (POLIMI)

Alessandra Cincinelli, Claudio Lubello, Andrea Bencini, Ilaria Colzi, Andrea Coppi, Sara Falsini, Simona Francalanci, Cristina Gonnelli, Riccardo Gori, Tania Martellini, Benedetta Pagliaccia, Alessio Papini, Laura Sforzi (UNIFI)

Daniela Ducci (UNINA)

Daniele Di Trapani, Gaspare Viviani, Alida Cosenza, Manuela Russo Tiesi (UNIPA)

Andrea Bottacin Busolin, Andrea Marion (UNIPD)

Paolo Ballirano, Giuseppe Capobianco, Marica Falzarano, Alice Marconato, Alessandro Pacella, Alessandra Polettini, Raffaella Pomi, Andreina Rossi, Silvia Serranti (UNIROMA1)

(Note: underlined names refer to critical-mass participants)

1 Technical references

Project Acronym	RETURN
Project Title	multi-Risk sciEnce for resilienT commUnities undeR a changiNg climate
Project Coordinator	Domenico Calcaterra UNIVERSITÀ DEGLI STUDI DI NAPOLI FEDERICO II domcalca@unina.it
Project Duration	December 2022 – November 2025 (36 months)

Deliverable No.	DV 4.3.1
Dissemination level*	PU, CO
Work Package	WP3 (VS4) - Enhancing capability to observe, model, and assess environmental hazards
Task	T 4.3.1 - Contaminant fate and transport models in water, groundwater and soils; innovative approaches to monitoring environmental pollution and quantification and reduction of uncertainty
Lead beneficiary	POLIMI/UNIFI
Contributing beneficiary/ies	POLIMI, UNIFI, UNINA, UNIPA, UNIPD, UNIROMA1

* PU = Public

PP = Restricted to other programme participants (including the Commission Services)

RE = Restricted to a group specified by the consortium (including the Commission Services)

CO = Confidential, only for members of the consortium (including the Commission Services)

1.1 Document history

Version	Date	Lead contributor	Description
0.1	05.02.2024-19.02.2024	All partners	Individual contributions to first draft
0.2	19.02.2024	Alessandra Polettini (task coordinator) (UNIROMA1)	First draft
0.3	21.02.2024–24.02.2024	All partners	Edits for approval
0.4	26.02.204	Manuela Antonelli (WP coordinator) (POLIMI)	Revision
1.0	29.02.2024	Alessandra Polettini (task coordinator) (UNIROMA1)	Final version

2 ABSTRACT

The present document provides details on the results/products of the activities conducted until month 15 in the framework of WP4.3 ("Enhancing capability to observe, model, and assess environmental hazards"), task T4.3.1 ("Contaminant fate and transport models in water, groundwater and soils; innovative approaches to monitoring environmental pollution and quantification and reduction of uncertainty").
In compliance with the executive working plan of the whole project, T4.3.1 involves using innovative techniques to detect and measure contaminants in different environmental compartments as well as in animal and plant organisms to provide the framework for risk assessment of anthropic activities. Target contaminants include microplastics (from both conventional plastics and bioplastics), elongated mineral particles (EMP), hydrocarbons, heavy metals, antibiotics, drugs, pesticides, and other contaminants of emerging concern (CECs). A range of methods including advanced analytical determination, lab-scale study, full-scale monitoring, modelling of transport and transformation mechanisms as well as uncertainty evaluation, are developed and used at different time/space scales to determine the evolution and transformation of contaminants in terrestrial water ecosystems, groundwater, and soils. The task is also complementary to the companion task T4.3.2 that focuses on the same issues for marine ecosystems.
The products of the investigation activities delivered at this stage of the project are grouped based on three main thematic areas:

1. **Development, application and validation of methods and protocols for the detection and quantification of contaminants in the environment:**
   i. advanced methodologies for microplastics and micro-bioplastics sampling and detection in biotic and abiotic samples (UNIFI, UNIROMA1);
   ii. advanced characterization of the interactions of hazardous (asbestos, erionite) and potentially hazardous (antigorite) mineral fibres with biological fluids of humans (UNIROMA1).
2. **Development, application and validation of methods for advanced environmental monitoring:**
   i. monitoring of microplastics in wastewater, groundwater and environmental compartments (UNIFI);
   ii. implementation of a hydrogeological database and field data collection for the detection of contamination and marine intrusion phenomena in coastal aquifers (UNINA);
   iii. development of advanced methods for the estimation of characteristics parameters in porous systems, streams and rivers for subsequent use in modelling (POLIMI, UNIPD);
   iv. development of advanced methods for holistic contaminant monitoring in urban water systems (including wastewater treatment plants, receiving water bodies, irrigation systems, soil, crops and humans) (POLIMI).
3. **Data analysis and modelling of transport, diffusion, transformation, degradation of contaminants as well as prediction of their effects on human health, flora, fauna and environment quality:**
   i. assessment of the impact of microplastics on plants, crops and stygofauna (UNIFI);
   ii. application of methods (based on statistical approaches, sensitivity analysis, uncertainty estimation) for the analysis of environmental data (UNINA, POLIMI);
   iii. development and validation of geochemical and hydraulic models describing reactive transport processes of contaminants in porous systems, streams and rivers (POLIMI, UNIPD);
   iv. risk-based modelling for the identification of the main sources and exposure routes of micropollutants released by combined sewer overflows or associated to the reuse of reclaimed wastewater in agriculture (POLIMI).

Efforts to efficiently integrate the multiple competences of the participants to T4.3.1 (encompassing the fields of chemistry, geology/mineralogy, hydrogeology, fluid mechanics, biology/botanic, civil and environmental engineering) have been made in order to attain the main target of WP4.3, involving the development of advanced methodologies and tools to observe, model and assess environmental hazards as thoroughly and comprehensively as possible. Taking further advantage from synergistic interactions among the multiple expertise involved will be the target of the future activities within the task that will lead to the final deliverable due at month 36 (DV 4.3.2 – "Multiscale modelling framework for contaminants transport and reaction with uncertainty quantification").

3 Table of contents

List of Tables

List of Figures

4 Improved methodologies for contaminant monitoring

4.1 Advanced methodologies for microplastic monitoring in biotic and abiotic samples (UNIFI)

(Contributors: Alessandra Cincinelli, Claudio Lubello, Andrea Bencini, Ilaria Colzi, Andrea Coppi, Sara Falsini, Simona Francalanci, Cristina Gonnelli, Riccardo Gori, Tania Martellini, Benedetta Pagliaccia, Alessio Papini, Laura Sforzi)

4.1.1 Introduction

The widespread occurrence and distribution of microplastics (MPs) in aquatic and terrestrial environments has become a problem of global concern. Nowadays, researchers employ diverse methods to sample, extract, separate and detect MPs by using their chemical and physical properties. A harmonization and standardization of analytical protocols for MPs analysis in aquatic ecosystems is currently a critical and mandatory scientific challenge. Furthermore, monitoring the MP presence in the environment and their impact on plants deserves attention considering that plants are fundamental primary producers and represent the starting point for bioaccumulation of MPs that can be transferred through the food chains. The consequences of MP presence in water and agricultural soils have not been properly elucidated so far. The abundance of these contaminants in edible parts of the plants and their effects in nutritional value and quality of fruits and vegetables is of paramount importance to assess the potential risk of human consumption of MPs from crops grown on contaminated soils.

4.1.2 Case study description

Comparative study for MP analysis in aqueous matrices. Three different methodologies, including LDIR (Laser Direct Infrared Imaging), micro-FTIR (2D imaging Fourier Transform Infrared spectroscopy coupled with microscopy) and Py-GCMS (pyrolysis–gas chromatography coupled with mass spectrometry), have been applied on standardized samples to compare and evidence strengths and weaknesses of each method, and then the more versatile one was applied on real samples. The occurrence of MPs in Italian wastewater and groundwater, their effects on groundwater invertebrate fauna, and their ability to infiltrate into bed sediments have been investigated.

Regarding the monitoring of the effects of MP pollution on plants, the impacts of MPs on growth, yield, physiology, and epigenetics has been investigated both in crop and water plants using model species.

4.1.3 Methodologies

4.1.3.1 Analytical methods

During the whole procedure of standard and sample preparation and analysis, strong attention was given to the quality control (i.e. potential air-borne plastic contamination, use of laminar-flow cabinets, fluorescent yellow TNT lab coats, metal or glassware, field and laboratory blanks, nitrile gloves at all times) to ensure the accuracy and reliability of results. Techniques such as LDIR, Py-GC/MS and micro-FTIR were performed to identify and characterize MPs in standard solutions and real samples such as wastewater, groundwater and plants.

For the study of MP effects on water plants, original and standard methods have been defined for the preparation and characterization of different types of MPs starting from original commonly used plastic materials. This gave the opportunity to have a more realistic blend of micro- and nano-particles to be administered to the plants in controlled conditions. A portable fluorometer (Handy-PEA) and a multi-pigment-meter (MPM-100) were used to carry out physiological measurements on photosynthetic

performance and pigment concentrations in leaves. The MSAP technique was also used to assess potential changes in DNA methylation levels induced by MPs.

4.1.3.2 Experimental methods

Development of methods and sampling methods.

- Homogeneous stock suspensions were prepared containing polyethylene (PE) and poly(methyl methacrylate) (PMMA) (Cospheric LLC) with specific size and concentrations (items/L).
- Collection of water in three Italian groundwater bodies was proposed along with collection of stygofauna pool samples (Figure 1). Samples were collected from two karst caves and two monitoring bores in an alluvial aquifer. A novel volume-reducing sampling device for MPs in groundwater, especially for hardly accessible sites (i.e., caves) was developed and optimized.
- Advanced methods for the sampling and characterization of MPs in wastewaters. Samples of influent and effluent were collected from different wastewater treatment plants (WWTPs), evaluating the influence of the sample volume to be processed on the detection and characterization of MPs in terms of analysis representativeness. The pretreatment procedure was fine-tuned to ensure the high-efficiency extraction of MPs (around 90 %) and their comprehensive characterization by dedicated analytical techniques. To this aim, samples were subjected to the following pretreatment steps: pre-concentration (vacuum-filtration, 5 µm mesh size, and recovery of the particles retained on the filter through backwashing), chemical digestion through Fenton reaction and extraction of MPs (vacuum-filtration, 5 µm mesh size, and recovery of the particles retained on the filter through backwashing).
- Solutions of MPs (size ~ 200-300 nm) were produced as water dispersions from PET bottles through repeated cycles of homogenization and used to prepare growth solutions at environmentally relevant concentrations. The solutions were tested to evaluate epigenetic effects on the model water plant Spirodela polyrhiza (Figure 2).
- The impact of MPs (PET and PVC) on crop health and fruit quality has been investigated using tomato (Solanum lycopersicum) as a model plant. Plants were grown in pots with an environmentally realistic concentration of MPs and photosynthetic parameters, number of flowers and fruits, plant biometry and ionome were evaluated, along with fruit quality (Figure 3).

4.1.4 Results

Recommendations and guidelines for quality control for MPs analysis were outlined.

- Advantages and limitations of LDIR, Py-GC/MS and micro-FTIR in terms for example of time of analysis, costs, sample preparation, identification of polymer type, quantification, limits of detection procedure were investigated.
- LDIR resulted to be an efficient technique for MPs detection and characterization in wastewaters. The analysis showed approximately a 90% removal of MPs in the WWTP water line, in agreement with literature data. The chemical nature and physical characteristics of the detected MPs depended on the origin of the treated wastewaters (i.e. municipal or industrial).
- A novel volume-reducing sampling device for MPs in groundwater was proposed.
- Evidence of MP presence in three Italian groundwater bodies. MP abundances were found to vary significantly between groundwaters, as well as between the corresponding groundwater taxa, while shape, colors, and size were comparable. Chemical characterization by micro-FTIR identified artificial/textile cellulose as the predominant polymer for each sample.
- The effects of polyethylene terephthalate (PET) MPs were tested on Spirodela polyrhiza and analysis showed decrease of photosynthetic efficiency, starch concentration, alterations in plant ionomic profile, and oxidative status. The DNA analysis showed unusual hypermethylation in 5'-GGGG sites showing for the first-time evidence of MP-induced epigenetic modifications in the plant world (Figure 2).

- The effects of PET and PVC MNPs in soils were tested on tomato plants. Results showed that MPs negatively impacted crop productivity and also fruit quality, with a reduction in the tomato nutritional values (Figure 3).

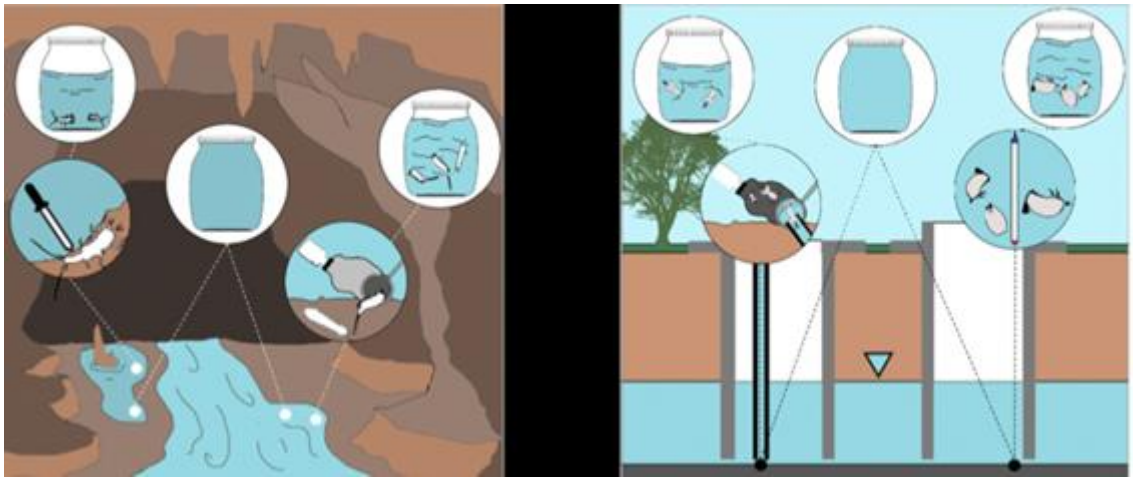

Figure 1: Schematic representation of the collection methods employed for faunal and water samples from karst cave (left panel) and alluvial bore (right panel).

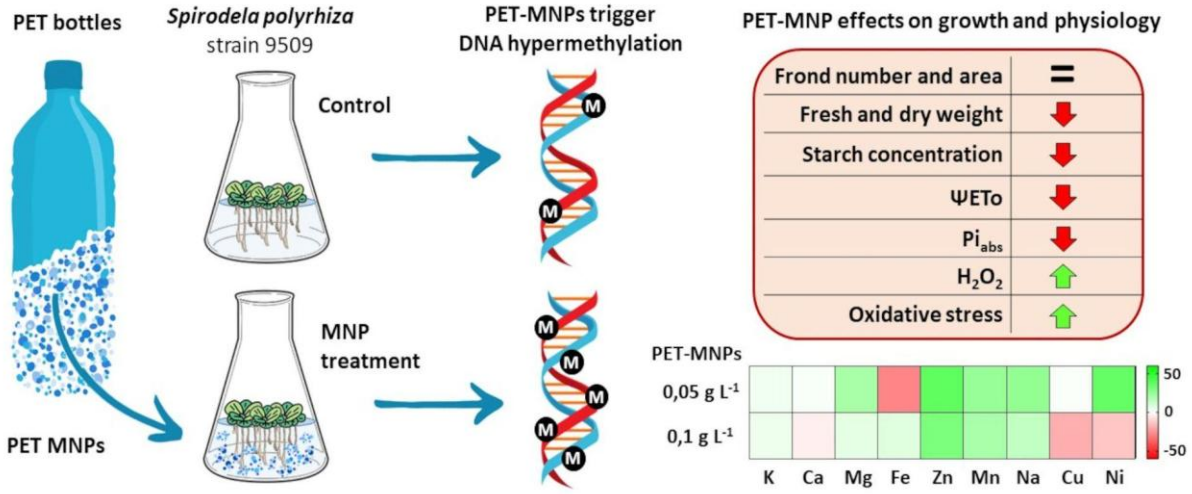

Figure 2: Schematic representation of the experimental setup and main results of the test on the water plant Spirodela polyrhiza.

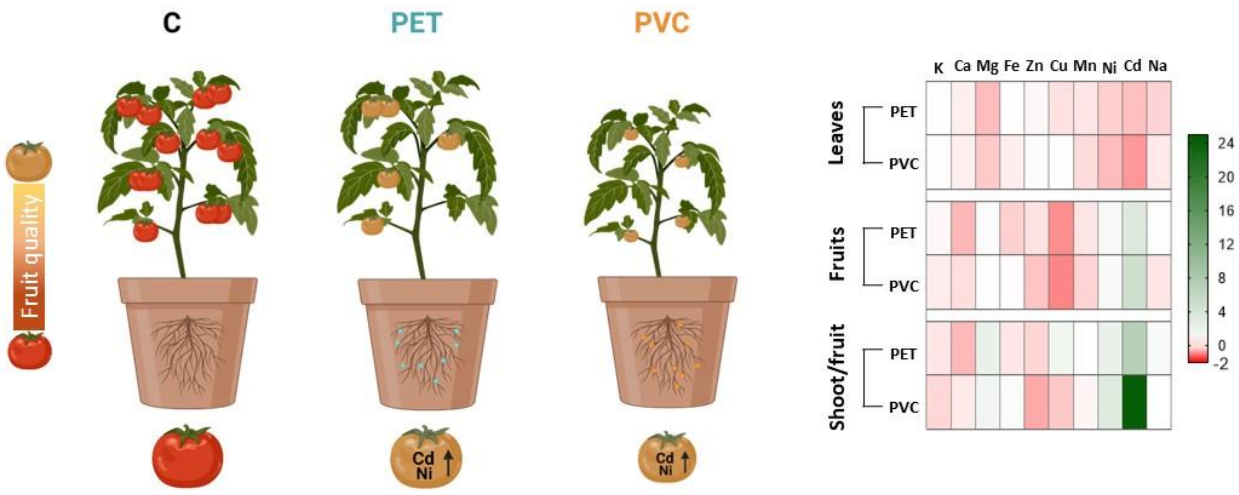

Figure 3: Schematic representation of the experimental setup and main results of the test on tomato plant (Solanum lycopersicum).

4.1.5 Scientific products and dissemination

26 – 30 June 2023 Poster presentation at the XXVII AIOL Conference in Naples "Characterization of (micro-)plastics in groundwater bodies : insights from Italian aquifers". Sforzi, L., Tabilio, A., Di Lorenzo, T., Balestra, V., Chelazzi, D., Ciattini, S., Martellini, T., Cincinelli, A.

2 – 7 July 2023 Oral presentation at the ICFS - International Conference on Fluvial Sedimentology "Experiments on Microplastic mobility into hyporheic zone" Mancini M, Francalanci S., Innocenti L., Solari L.

Can microplastics threaten plant productivity and fruit quality? Insights from Micro-Tom and Micro-PET/PVC. Dainelli M., Pignattelli S., Bazihizina N., Falsini S., Papini A., Baccelli I., Mancuso S., Coppi A., Castellani M.B., Colzi I., Gonnelli C. Science of the Total Environment 2023, https://doi.org/10.1016/j.scitotenv.2023.165119

1 - 2 September 2023 Poster presentation at the Symposium CSGI in Naples "Effect of micro-nanoplastics from airborne pollution on *Tillandsia usneoides* as a green biosensor" Falsini S., Colzi I., Chelazzi D., Dainelli M., Schiff S., Papini A., Coppi A., Gonnelli C., Ristori S.

08 September 2023: Workshop Nell'Orto Botanico di Firenze: Organizzazione evento sulla dispersione delle plastiche nell'ambiente e loro controllo attraverso corretti metodi di raccolta e recupero all'apertura della mostra dell'artista Annarita Serra.

08 September 2023, Oral presentation within the workshop Serra in serra: le opere sostenibili di Annarita Serra in mostra all'Orto botanico di Firenze "Microplastiche, un inquinante emergente nelle acque sotterranee" Sforzi, L., Tabilio, A., Di Lorenzo, T., Balestra, V., Chelazzi, D., Martellini, T., Cincinelli, A.

08 September 2023, Oral presentation within the workshop Serra in serra: le opere sostenibili di Annarita Serra in mostra all'Orto botanico di Firenze Gli impatti delle micro e nanoplastiche sulle piante Falsini S., Colzi I., Dainelli M., Coppi A., Papini A., Ristori S., Gonnelli C.

13- 16 September 2023 Poster presentation at the 118th Congress of the Italian Botanical Society (IX INTERNATIONAL PLANT SCIENCE CONFERENCE) "Airborne pollution effects on *Tillandsia usneoides* induced by iron oxide nanoparticles" Falsini S., Colzi I., Dainelli M., Parigi E., Schiff S., Papini A., Talbot D., Abou-Hassan A., Gonnelli C., Ristori S.

30 September 2023: student seminar on the project activities and results during the exhibition of the Annarita Serra's works in the Orto Botanico di Firenze and the Bright Night in Florence. This event will be entitled: Dal "riciclo ad arte" alla scienza per l'economia circolare.

23-26 January 2024 Oral presentation at the 3rd PiCSU symposium at Unifi "Evidence of microplastics (MPs) in ground- and well- waters: from sampling to analysis" Sforzi, L., Tabilio, A., Di Lorenzo, T., Martellini, T., Cincinelli, A.

Growth, physiological parameters and DNA methylation in *Spirodela polyrhiza* (L.) Schleid exposed to PET micro-nanoplastic contaminated waters. Dainelli M., Castellani M.B., Pignattelli S., Falsini S., Ristori S., Papini A., Colzi I., Coppi A., Gonnelli C. Plant Physiology and Biochemistry 207, 108403. https://doi.org/10.1016/j.plaphy.2024.108403

"Investigations on microplastic infiltration within natural riverbed sediments" M. Mancini, S. Francalanci, L. Innocenti, L. Solari. Science of the Total Environment, 904 (2023) 167256, https://doi.org/10.1016/j.scitotenv.2023.167256.

(Micro-)plastics in saturated and unsaturated groundwater bodies: first evidence of presence in groundwater fauna and habitats. L. Sforzi, A. Tabilio Di Camillo *, T. Di Lorenzo, D. M. P. Galassi, V. Balestra, L. Piccini, S. B. Cabigliera, S. Ciattini, M. Laurati, D. Chelazzi, T. Martellini, A. Cincinelli. Sustainability-2846084, major revisions

4.2 Classification of Mater-Bi® bioplastics in anaerobic sludge by SWIR hyperspectral imaging (UNIROMA1)

(Contributors: Giuseppe Capobianco, Marica Falzarano, Alessandra Polettini, Raffaella Pomi, Andreina Rossi, Silvia Serranti)

4.2.1 Introduction

Biodegradable plastics are currently replacing commodity plastics in various applications, including disposable tableware. One of the most common blends on the market is Mater-Bi® (MB), a family of polymeric compounds based on TPS and commercialized with different chemical formulations depending on the used co-polymer (Bracciale et al., 2024). The main advantage of biodegradable products is the possibility to apply biological processes (such as anaerobic digestion) in the end-of-life and treat them together with the organic fraction of municipal solid waste (OFMSW) using the already existing facilities. However, a comprehensive understanding of bioplastics' behaviour under a variety of environmental conditions is currently missing and the efficiency of the co-digestion with organic waste is still under examination (Cazaudehore et al., 2022; Falzarano et al., 2023). Full-scale digesters may need technical improvements to treat bioplastics and OFMSW while maintaining the quality of the final digestate (Calabrò and Grosso, 2018).

One of the aspects of concern related to the combined treatment of bioplastic residues and the organic fraction of municipal waste is the potential generation of byproducts (including micro-bioplastics) during the biodegradation process, which could persist in the digestate and be released into the environment upon soil application. This may create potential risks to vegetation and crops, in turn with further potential risks to human health along the food chain.

A systematic and comprehensive assessment of bioplastics biodegradation is needed and should be completed with a quality assessment of the final compost/digestate. In particular, monitoring the evolution of bioplastics degradation and investigating the formation of byproducts during biodegradation need careful evaluation in terms of concentration, nature and potential toxic effects of the biodegradation products. It is thus important to develop adequate methodologies to identify the presence of degradation products including residual micro-bioplastics in compost and digestate from biological processing of organic waste. The development of accurate and reliable identification methods of micro-bioplastics in such systems poses several challenges, due to the high heterogeneity of the matrix and the masking effects caused by the bulk of the organic matrix. Within this framework, an innovative approach to monitor the behaviour of some disposable biodegradable cups during anaerobic digestion was developed using hyperspectral imaging (HSI), with particular emphasis on detecting micro-bioplastics generation during the process.

4.2.2 Methodologies

The aim of the study was to overcome the challenges for micro-bioplastics identification in digestate. The study consisted of two consecutive experimental phases. The first phase's aim was to analyze the degradation process of single-use bioplastic products in an anaerobic environment under thermophilic conditions, while the second part focused on developing a fast and efficient methodology capable of identifying residual plastic fragments within the digestate resulting from the degradation tests.

4.2.2.1 Experimental methods

MB cups compliant with EN13432 were acquired and characterized to investigate their polymeric matrix and the main chemo-physical characteristics. Then the cups were manually cut in squares 1.5×1.5 cm removing the bottoms and the edges to ensure material homogeneity. An anaerobic inoculum was sampled from a full-scale digester, and it was sieved at 0.84 mm to remove the coarser fraction. Reactors were filled with 400 g of a MB/inoculum mixture at a ratio of 1 gVS/gVS or with the sole inoculum (blank) and were flushed with nitrogen to ensure anaerobic conditions. In addition, positive control tests were performed using calcium lactate to evaluate both the effectiveness of the inoculum and the reliability of the experiment. As

a term of reference, according to ISO 14853 (ISO 14853:2016), a test is considered valid if the biodegradation of the reference material exceeds 70% within 60 days. All tests were run in duplicates. The reactors were incubated in a thermostatic bath at 55 °C and tested both at fixed reaction time (15, 24 and 32 days) and until reaching a plateau. The biogas evolution in time was monitored in terms of volume and composition. The degree of biodegradation was calculated using Equation 1:

$$Biodegradation\ (t) = \frac{P_{net}(t)+P_{ICnet}\ (t)}{P_{th}} \quad (1)$$

where $P_{net}(t)$ is the actual cumulative biogas production (net of blank) at time t, $P_{IC}(t)$ is the actual dissolved inorganic carbon (IC) (net of blank), P_{th} is the theoretical biogas production calculated according to the Buswell equation (Buswell and Mueller, 1952), which is commonly employed to estimate the stoichiometric quantity of biogas production under the assumption of complete conversion of the original material. Bioplastics mass loss was investigated by sieving the digestate at 0.84 mm. The bioplastic fragments retained on the sieve were then washed with deionized water and dried at 30 °C until constant weight. At the end of the biodegradation tests, an aliquot of the digestates was filtered on paper filters (porosity 1.2 µm) to create a thin layer, which represented the validation set for the hyperspectral analysis. The degraded bioplastic fragments coming from the mass loss analysis were used as well, to retrieve information on the MB spectra changes at different moments of the process. In addition, clean MB cups were powdered at different size ranges (0 – 0.5, 0.5 – 1 and 1 – 5 mm), placed over the filters with the sole inoculum and used as training set.

4.2.2.2 Analytical methods

To test the applicability of the analytical technique for micro-bioplastics identification, hyperspectral images of the filters were acquired in the short-wave infrared range (SWIR: 1000-2500 nm) using Specim SISUChema XL™, equipped with an ImSpector™ N25E imaging spectrograph (Specim Ltd, Finland), with a spectral sampling/pixel of 6.3 nm, coupled with a MCT camera (320 × 240 pixels). The selected configuration for the image acquisitions covers a maximum field of view of 1 cm with a pixel resolution of 30 µm. The spectral analyses were carried out using the PLS_Toolbox (Version 7.8 Eigenvector Research Inc.), running inside Matlab (Version R 2021b, The Mathworks Inc.). Different pre-processing strategies (i.e. scatter correction methods and spectral derivatives), following the combination widely adopted in the literature (Rinnan et al., 2009), were selected in order to optimize recognition of MB. Data exploration, based on Principal Component Analysis (PCA) was carried out. PCA is a powerful and versatile method capable to provide an overview of complex multivariate data and it is widely adopted to treat HSI data (Amigo et al., 2013). Finally, a Partial Least Squares-Discriminant Analysis (PLS-DA) classification model (Ballabio et al., 2013) was built for the identification of MB in the sludge. More in details, a 3-classes model was built, to identify the background (filter), the inoculum (blank) and the MB particles.

4.2.3 Results

The selected MB cups were mainly composed by polylactic acid (PLA) and polybutylene succinate (PBS) with some talc fillers. After 43 days the cups reached 43% biodegradation degree, which was mainly imputable to the PLA fraction. Around 70% of the initial bioplastic material was found to have a >0.84-mm size.

Concerning the results obtained by HSI, Figure 1a shows the false color image with the selection of the 3 classes, MB, inoculum (blank) and background (filter), respectively. Figure 4b shows the different spectral signatures of the three set classes and, finally, the PCA score plot (Figure 1c) confirms the possibility to identify the three classes, showing three different clusters corresponding to MB, inoculum and background, respectively, despite the high variability of the inoculum.

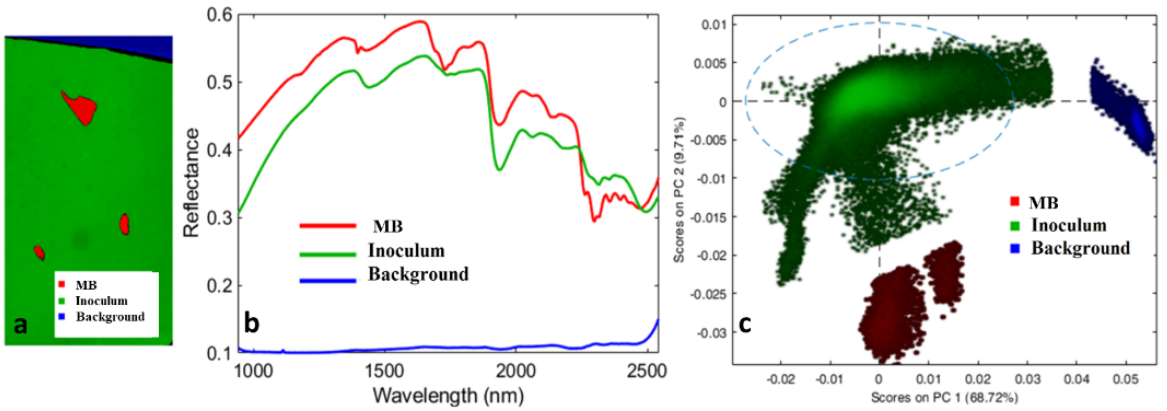

Figure 4. False colour image with set classes: MB, inoculum and background (a), average raw reflectance spectra of the 3 classes (b) and corresponding PC1-PC2 score plot (c).

Figure 5 shows the prediction results obtained by PLS-DA classification for the MB, inoculum and background classes of the validation dataset. An excellent classification is reached for the MB class, allowing the identification of micro-bioplastics even smaller than 100 µm.

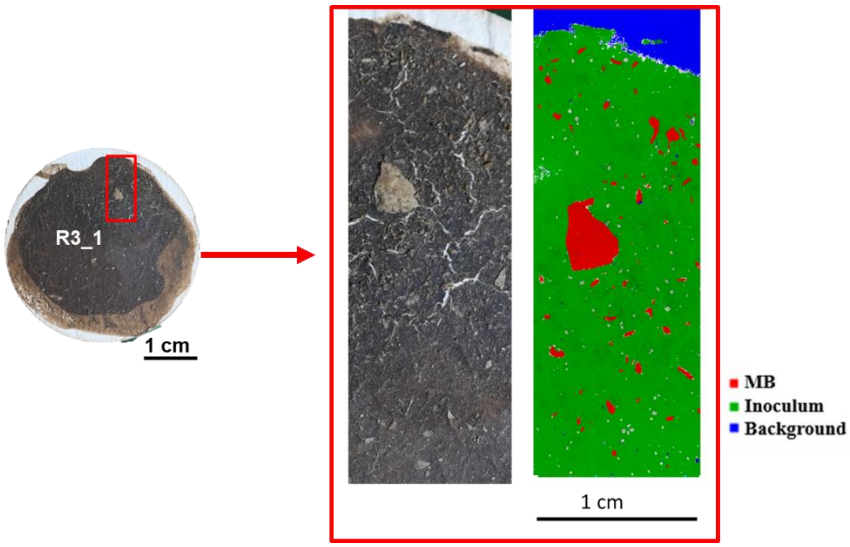

Figure 5. PLS-DA classification results: source image and false colour prediction image of the validation dataset.

4.2.4 Scientific products and dissemination

Papers on international journals:

Falzarano, M., Polettini, A., Pomi, R., Rossi, A., Zonfa, T., 2023. Anaerobic Biodegradability of Commercial Bioplastic Products: Systematic Bibliographic Analysis and Critical Assessment of the Latest Advances. Mater. 2023, Vol. 16, Page 2216 16, 2216. https://doi.org/10.3390/MA16062216

Conference and workshop proceedings:

Capobianco G., Falzarano M., Bonifazi G., Polettini A., Pomi R., Rossi A., Serranti S., Classification of Mater-Bi® bioplastics in anaerobic sludge by SWIR hyperspectral imaging, Dissemination Workshop RETURN, Torino, 1-2 February 2024.

Falzarano M., Capobianco G., Bonifazi G., Bracciale M.P., Polettini A., Pomi R., Rossi A., Sarasini F., Serranti S., Tirillò J., Zonfa T., Metodologie per la valutazione della biodegradabilità di prodotti in bioplastica, Workshop SHARESCIENCE2024, Sapienza University of Rome, 15-16 February 2024.

Giuseppe Capobianco, Marica Falzarano, Giuseppe Bonifazi, Alessandra Polettini, Raffaella Pomi, Andreina Rossi, Silvia Serranti. Characterization of disposable Mater-Bi® bioplastic by hyperspectral imaging for anaerobic biodegradation monitoring, to be presented to the SPIE Defence and Commercial Sensing Conference (Washington, 21-25 aprile 2024).

4.3 Prototypal quantification, by flow through reactors, of the kinetics of the dissolution process, in different types of simulated human lung fluids, of elongated mineral particles (EMP) from different outcrops (UNIROMA1)

(Contributors: Paolo Ballirano, Giuseppe Capobianco, Alice Marconato)

4.3.1 Introduction

Asbestos fibres are easy to inhale through airways to pulmonary alveoli. Lung carcinoma (LC) and malignant pleural mesothelioma (MPM) are the two thoracic tumours associated to asbestos exposure. Even though asbestos production and use has been banned in Italy since 1992, many contaminated sites are still present, and many ex-exposed workers are still at risk to develop cancer due to the long latency period. Furthermore, ban and regulations cannot be applied to naturally occurring asbestos (NOA), where weathering events and/or anthropic activities may disturb NOA-bearing outcrops, thus provoking the formation of potentially inhalable fibres. In recent years attention encompassed other types of elongated mineral particles that may share similar morphological features with asbestos, while differing in mineralogy (naturally occurring non-asbestos: NONA)), such as erionite and antigorite, whose exposure has been linked to high incidence of LC and MPM. More than 400 mineral species occur under an elongated habit, and they are widespread in Italy. In detail, NOA have been observed in at least 10 Italian regions and this number is possibly higher. The planned research activities consist of the prototypal quantification, by flow through reactors, of the kinetics of the dissolution process, in simulated human lung fluids, of several NOA and NONA from different Italian outcrops. This approach will provide more accurate estimation of bio durability and lifetime, commonly calculated from close system experiments, that are important parameters for triggering different diseases. Characterization at the atomic scale, by a multi analytical approach, of the pristine and leached fibres will be used as background for building 3D dissolution models and to correlate with chemical reactivities. The well-established use of simulated lung fluids (SLFs) as an *in vitro* technique to predict the possible *in vivo* behaviour of inhaled elongated mineral particles (EMPs) represents an oversimplification due to the lack of specific components that may affect the dissolution mechanisms and biological activity of inhaled fibres. Understanding the interaction of hazardous (asbestos, erionite) and potentially hazardous (antigorite) mineral fibres with biological fluids (BFs) of the lung and pleural compartments is expected to provide a significant advancement of knowledge on the interaction between EMPs and the biological environment.

4.3.2 Case study description

To build a self-consistent database of the kinetic of the dissolution process of standard samples during incubation in SLFs in close system experiments, the behaviour of Union for International Cancer Control (UICC) amosite sample, a fibrous amphibole. In particular, the surface modifications of amosite fibres during incubation in a mimicked Gamble's solution (MGS) at pH 4.5, were monitored up to one month. The kinetic of dissolution in SLFs of crocidolite and tremolite, two other fibrous amphiboles, has been recently investigated using the same methodological approach described in the following.

4.3.3 Methodologies

Leached fibres were studied by a multi-analytical approach: field-emission scanning electron microscopy (FE-SEM) was used to characterize the fibre morphology, inductively coupled plasma optical emission spectrometry (ICP-OES) was employed to measure the cation release into the leaching solution. The analytical approach based on X-ray photoelectron spectroscopy (XPS), exploited for characterizing the other asbestos fibres, was here adapted to monitoring possible changes of surface chemistry, and includes the Fe speciation of the amosite. Powder X-ray diffraction (PXRD) and high-resolution transmission electron microscopy (HR-TEM) were used to observe possible nanostructural modification of the fibres.

4.3.3.1 Analytical methods

A sample of amosite (fibrous grunerite) standard sample from Penge mine (South Africa), supplied by the Union International for Cancer Control (UICC), was investigated. Its empirical formula is: $^{A}(Na_{0.02})_{\Sigma 0.02}{}^{B}(Fe^{2+}{}_{1.54}Mn_{0.29}Na_{0.10}Ca_{0.07})_{\Sigma 2.00}{}^{C}(Fe^{2+}{}_{2.92}Mg_{1.93}Fe^{3+}{}_{0.15})_{\Sigma 5.00}{}^{T}(Si_{7.93}Al_{0.07})_{\Sigma 8.00}O_{22.00}{}^{W}(OH_{2.00})_{\Sigma 2.00}$. Rietveld refinement results evidenced that Fe^{2+} is allocated in the octahedral layer following the site preferences M(1) ≈ M(3) > M(2), whereas Mg is preferentially ordered at M(2). Quantitative Phase Analysis indicates about 10 wt.% of accessory phases including quartz (ca. 4 wt.%), ankerite (ca. 1 wt.%) and traces of stilpnomelane and biotite/annite. The surface area of the samples, measured by nitrogen physisorption (BET), resulted to be 4.5 $m^2 \times g^{-1}$.

4.3.3.2 Experimental methods

Dissolution experiments were carried out under static conditions, in the same experimental conditions used for UICC crocidolite and fibrous tremolite [18]. Briefly, samples were incubated (20mg) in MGS (40 mL) at pH 4.5, kept at 37 °C up to 1 month under gently shaking. Aliquots of the suspension were filtered on nitrocellulose filter membranes (porosity of 0.22 µm) and analysed by ICP-OES using a Perkin–Elmer Optima 2000 DV ICP-OES spectrometer (Perkin-Elmer, USA). To remove any residues of the solution, the fibres deposited on filters were rinsed with ultrapure deionized water and then stored under argon prior to the SEM, TEM, XRPD, and XPS investigations. SEM images were acquired by a Field Emission (FE) SEM Zeiss Gemini 500 (Germany). Samples were mounted on a stub with conductive carbon tape and a 5 nm of chromium film was deposited on the sample surface to make it conductive during measurements. TEM analysis was done using a JEOL JEM-2010 (Japan) microscope operating at 200 kV, equipped with a LaB_6 source, an Energy Dispersive System (EDS) (Oxford ISIS, UK) for microanalysis, and an Olympus Tengra CCD camera (2k x 2k x 14 bit) for image acquisition. Aliquot of samples (pristine amosite and 1 month in MGS incubated amosite) were pipetted on 200 mesh Cu-grids supported with holey carbon film, and then carbon-coated to increase conductivity. Powder X-ray diffraction (PXRD) data were collected on a D8 Advance (Bruker AXS, Karlsruhe, Germany) running in θ/θ transmission mode using a capillary as sample holder. The sample incubated for 1 month in MGS (A-720h) was loaded in a 0.5 mm diameter borosilicate glass capillary. The instrument is equipped with an incident beam focusing graded multilayer Göbel mirror and a PSD VÅntec-1. The diffraction pattern was measured in step-scan mode, using CuKα, in the 6-145° 2θ angular range, 0.022° 2θ step size and 20 s counting time. XPS investigation was carried out by a Theta Probe X-ray photoelectron spectrometer (Thermo Fisher Scientific, Waltham MA, USA), equipped with a flood gun neutralizer for charge compensation. All the spectra were acquired using Al Kα1,2 source (hν = 1486.6 eV) and a 400 µm spot size. The analyser operated in the fixed analyser transmission (FAT) mode, with pass energy (PE) set at 200 eV and at 100 eV for the survey spectra and for the high-resolution spectra, respectively. The linearity of the binding energy scale was checked by periodic calibration following ISO 15472:2014. The binding energy scale was referred to the signal at 285.0 eV of adventitious aliphatic carbon.

4.3.3.3 Modelling approaches

PXRD data were evaluated by the Rietveld method using Topas V6 which uses the Fundamental Parameters Approach (FPA) for describing the peak shape. Preliminary scrutiny of the pattern indicated the persistence of the same phases at the minor/trace level reported in reference data and the same computational procedure was applied. Quartz, ankerite and garnet were included to the Rietveld refinement. Differently, the main reflection of stilpnomelane and biotite/annite were approximated by two peaks not related to any structure whose position, intensity and breadth were also refined. Only scale factors, cell parameters and peak shapes were refined for quartz, ankerite and garnet. The structure of amosite was refined keeping all displacement parameters fixed to reference data and no restraints on bond distances and angles were imposed. Site scattering (s.s.) at M(1), M(2), M(3) and M(4) was optimized. Neither split M(4') site nor A-type sites were observed. The refinement was performed using the normalized symmetrized spherical harmonics functions for describing the anisotropic peak broadening of the diffraction pattern. Absorption correction was performed using the equation of Sabine et al. for a cylindrical sample and the presence of preferred orientation was modelled using normalized symmetrized spherical harmonics functions (4th-order, eight

refinable parameters. The surface fibre composition determined by XPS, was reported in atomic percentages, and it was calculated correcting the peak area for Scofield's photoionization cross-sections, the asymmetry function, the transmission function correction, and the attenuation length. Data are reported as the average values of three different analysed areas, with standard deviation in brackets.

4.3.4 Results

FE-SEM images indicate that amosite fibres, similarly to crocidolite fibres, are straight and rigid, and are arranged in bundles of variable dimensions of ca. 1-5 μm × 20-1000 μm having split ends consisting of fibrils of nanometric diameter (ca. 150-300 nm) with partially irregular surface, indicating the possible occurrence of an amorphous layer due to weathering processes. Moreover, after immersion in MGS up to 1 month in rare cases some effects of the dissolution are evident on the fibres, being their surface more lobate and irregular with respect to that of the starting material. TEM observations reveal similar nanostructures for pristine and treated samples. Fibre size and aspect ratio are highly variable, with maximum diameter of 500-600 nm. High-magnification images reveal the constant occurrence of an ultrathin amorphous film, approximately 10-30 nm wide surrounding amosite fibres, occurring also at fibre terminations (Figure 6). The only remarkable difference between pristine amosite and treated fibres is an average increase in the amorphous film thickness at fibre termination in the treated sample (up to 25 nm), where rare irregular, wavy lattice fringes may occur, and suggesting possible precipitation of smectite-like layers. PXRD indicate that cell parameters and volume of the treated sample are very close to those of pristine. We observed the complete dissolution of ankerite [calcium, iron carbonate: $CaFe(CO_3)_2$] found in the pristine sample. Moreover, the presence of an extra reflection at ca. 18° 2θ, already observed for other amphiboles upon dissolution experiments in MGS at acidic conditions (UICC crocidolite and tremolite) was assigned to newly precipitated hydrated sulphates. No significant structural variations at the bulk level were observed from the structure refinement by the Rietveld method possibly limited to a minor oxidation of Fe^{2+} at C sites ICP-OES analyses after fibre incubation in the MGS indicate that Si and Mg release shows a parallel trend, both increasing with incubation time, from 57(1) mg/kg up to 2169(62), and from 394(3) mg/kg up to 985(36) mg/kg, respectively. Ca and Fe release mainly occurs in the first stages of dissolution (48 and 24 hours of incubation, respectively). The observed release of Fe and Ca may be attributed to the dissolution of ankerite in the hand sample, in agreement with PXRD results showing the absence of this accessory phase in the sample incubated up to 1 month in MGS. It must be pointed out that the concentration of released Ca is higher than that expected from the dissolution of only ankerite. Thus, due the occurrence of small content of Ca in the amosite structure, Ca leaching from the fibres cannot be ruled out. Moreover, the small amount of Fe detected in the solution (up to 720 mg/kg) indicates possible formation of Fe-bearing secondary phases (hydrated sulphates), as revealed by PXRD data. This hypothesis is further supported by the absence of Fe in the solution for longer incubation times (1 month). The XPS survey spectra of amosite samples after suspension in MGS show the presence of Si, O, Fe, Mg, Ca, and Na, together with C due to the presence of the adventitious carbon caused by the contact with the laboratory atmosphere and aqueous solutions. Specifically, no S and Cl signals that might be due to the incubating solution were found on the fibre surface. The high-resolution spectra were processed to gain data on the chemical state of the elements. Si 2p peaks were fitted with a doublet due to spin orbit coupling. The energy separation between the $2p_{3/2}$ and $2p_{1/2}$ components and their area ratio were constrained to 0.8 and 2:1, respectively. The binding energy of Si $2p_{3/2}$ was found to be in the range 102.5 (0.1) – 102.7 (0.1) for the considered samples and agrees with those reported in previous investigations. Oxygen O 1s peak resulted to be multicomponent with a signal due to oxygen in oxides in the range 530.0-530.2 eV, the component due to bridging oxygen is at 532.2 eV and the component assigned to non-bridging oxygen in silicates and -OH are found at about 531.2 eV. Compared to the bulk composition, an enrichment in Mg and Si with respect to Fe is evident on the surface of pristine fibres, likely due to weathering processes, as we already observed for UICC crocidolite fibres. The Fe $2p_{3/2}$ signals were resolved in three components assigned to: i) Fe(II) bound to oxygen with its satellite, at about 709.0 eV ii) Fe(III) bound to oxygen found at 710.6 eV, and iii) FeOOH at 711.7 eV. Significant variations of the Fe components were observed only in the first hour of sample incubation in MGS. In particular, the intensity of the Fe(II)-O signal decreases from ca. 70% of the total peak area in the pristine sample down to ca. 60%, at the expense of the Fe(III)-O signal, which increases from ca. 3% up to ca. 18%. Moreover, signals keep almost constant up to the end of the experiment. Comparing the Si/Mg ratio of the leached cations at the various sampling times with that retrieved from surface chemical analysis,

a preferential Mg release from the amosite fibres is evident, especially in the first 48 hours, as already observed for the dissolution of asbestos tremolite and UICC crocidolite samples. Accordingly, the incongruent behaviour of the dissolution process was also highlighted by XPS results showing a depletion of Mg and Ca on the surface of the leached fibres, in agreement with their Madelung site energies in the amphibole structure. The Fe enrichment on the fibre surface indicates no Fe leaching from the amosite fibres in the adopted experimental conditions (pH of 4.5 and atmospheric pO_2), despite significant Fe(II) occurrence at the M(4) site, where cations are expected to be rapidly leached out during amphibole dissolution on the basis of its Madelung site energy. Concerning Fe speciation, pristine fibres show a more oxidized surface with respect to the bulk, with Fe(III) mainly present as FeOOH. For the MGS incubated samples, the intensity of the Fe(II)-O component decreases in the first hour of incubation, counterbalanced by the increase of the Fe(III)-O component. Besides, the increase of the Fe(III)-O component on the surface is in agreement with the increased oxygen content observed in the same interval of time. The depletion of Fe(II) centres on the surface indicates that for amosite fibres the Fe oxidation is faster than the fibre dissolution in the first hour of incubation, similarly to what was observed for samples of fibrous tremolite. However, for amosite fibres the Fe(II) reduction is less marked, being only ca. 17% of the total surface Fe(II), whereas for tremolite is much more pronounced. Moreover, in the asbestos tremolite sample the oxidation converted Fe(II) into FeOOH, very likely located in the outer part of the sample surface. This might be attributed to the slow dissolution rate of the investigated fibres, affected by both their crystal chemical features and low surface area (ca. 2.7 $m^2 \times g^{-1}$ for Maryland tremolite). Notably, the observed trend is opposite to that of UICC crocidolite, which shows an increase of the Fe(II) component coupled with a decrease of the FeOOH component. This is a consequence of the fast fibre dissolution that removes the outer layer and promotes the exposure of new Fe sites from the bulk, especially in the form of Fe(II) of which the bulk is enriched with respect to the surface. Considering that for amosite fibres the FeOOH component keeps constant with incubation time, the moderate conversion of Fe(II)-O to Fe(III)-O observed in the first hour of incubation may be interpreted as the result of both the oxidation of the Fe centres initially present on the fibre surface and those emerging from the bulk following mineral dissolution. Those interpretations are supported by the Rietveld structural analysis that indicates a minor oxidation of Fe(II) of the bulk. The lower surface area of amosite (ca. 4.5 $m^2 \times g^{-1}$) with respect to that of crocidolite (ca. 8.7 $m^2 \times g^{-1}$) likely hinders a sustained occurrence of Fe(II) centres on the fibre surface. This agrees with previous results obtained on two fibrous tremolite samples with largely different surface area revealing that both the processes of dissolution and surface modification are slower for the sample with lowest surface area. Moreover, starting form 24 hours of sample incubation an equilibrium between Fe oxidation rate and fibre dissolution kinetics is established. To make a comparison of the biodurability among these amphibole asbestos samples, the dissolution rate of amosite fibres normalized to their surface area was quantified using the Si release in the unsaturated region (0-48 h). The value obtained was $dSi/dt = 0.002\ \mu mol \times h^{-1} \times m^{-2}$, in between that retrieved from UICC crocidolite and asbestos tremolite ($dSi/dt = 0.007\ \mu mol \times h^{-1} \times m^{-2}$ and $0.0004\ \mu mol \times h^{-1} \times m^{-2}$, respectively). This result unequivocally confirms previous findings postulating: i) a quicker dissolution for Fe rich silicates with respect to their isostructural, iron-free analogues; ii) asbestos tremolite durability is among the highest compared to any other amphibole asbestos.

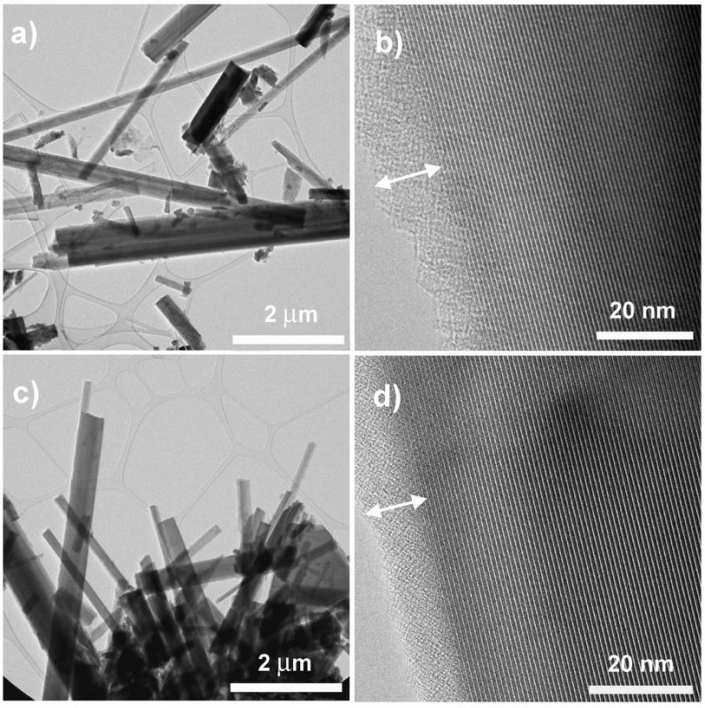

Figure 6: Bright-field TEM images of pristine amosite (a and b) and amosite after 1 month of incubation (c and d), at variable magnification. Lattice fringes in b) and d) correspond to (020) with d-spacings of 9.05-9.20 Å. Double-arrowed white lines highlight the thin amorphous film, surrounding both pristine and treated amosite fibres.

4.3.5 Scientific products and dissemination

Pacella, A., **Ballirano, P.**, Di Carlo, M.C., Fantauzzi, M., Rossi, A., Nardi, E., Viti, C., Arrizza, L., Campopiano, A., Cannizzaro, A., Bloise, A., Montereali, M.R. (2023) – *Dissolution reaction and surface modification of UICC amosite in mimicked Gamble's solution; a step toward filling the gap between asbestos toxicity and its crystal chemical features.* Nanomaterials, **13**, 02933. DOI:10.3390/nano13222933

Petriglieri J.R., Pacella A., Barale L., Leinardi R., Tomatis M., **Ballirano P.,** Piana F., Haux F., Campopiano A., Turci F. (2023) – *An integrated general approach to assess the potential risk of outcrops contaminated by asbestos and asbestos-like minerals*, In EGU General Assembly 2023, Vienna 23-28/04/2023.

Turci F., Petriglieri J.R., Barale L., Gazzano E., Aldieri E., Tomatis M., **Ballirano P**., Piana F., Pacella A., Campopiano A. (2023) – *Toward a general approach to risk assessment of naturally occurring asbestos and asbestos-like minerals: the case of fibrous antigorite*, In Inhaled Particles and NanOEH Conference 2023, London 15-18/05/2023.

Marconato A. (2024) – *Elongated mineral particles in biological fluids: a possible key for modelling their in vivo behaviour*. In Roma chiama Roma 2024, Rome 22-23/01/2024.

4.4 Analysis and implementation of methodologies to detect contamination and marine intrusion phenomena in coastal aquifers (UNINA)

(Contributor: Daniela Ducci)

4.4.1 Introduction

The European Water Framework Directive (2000/60/EC) and Groundwater Directive (2006/118/EC) require member states to identify groundwater bodies and monitor their qualitative and quantitative status. Therefore, a comprehensive knowledge on groundwater bodies characteristics, groundwater quality and groundwater availability should be achieved for a sustainable management of water resources. In complex hydrogeological settings and in areas characterised by widespread anthropic activities (i.e., agricultural and livestock activities) and urban settlements, such knowledge is usually represented by a huge amount of data, often non-homogeneous in terms of spatial and temporal distribution. In this context, the coastal areas of the Mediterranean area are subjected to significant environmental stress linked to the simultaneous presence of urbanized areas, sometimes densely populated, agricultural fields (seed and fruit), livestock farms and industrial activities. Moreover, groundwater and surface water represent a resource of considerable value for water supply. Groundwater constitutes a strategic resource as, compared to surface water, it is more protected from the contamination of pollutants and less influenced by extreme events, such as local droughts or intense rainfall, and climate change at a global level. Nonetheless, groundwater is also a vulnerable resource from both a quantitative and qualitative point of view, with ever-increasing risks in environmental contexts strongly influenced by both natural processes and anthropic activities capable of transforming the territory and the ecosystems connected to it. Therefore, it is of considerable importance to investigate the processes and causes that have an impact on the quality and quantity of groundwater resources. Coastal areas represent a context in which it is also necessary to investigate and prevent the phenomenon of marine intrusion into coastal aquifers in order to correctly protect and manage the water resource itself.

The objectives of this study are: to implement an interactive hydrogeological geo-database for the optimization of the handling and storage of spatio-temporal data for the Volturno Plain in Campania Region (Southern Italy); to study the phenomena of salt intrusion and human contamination in the same area by the application of advanced statistical analyzes of hydrochemical data for the identification of natural/anthropic phenomena and geochemical processes.

4.4.2 Case study description

The area of interest is located in the northern part of Campania Region (Southern Italy) and it mainly includes the Groundwater Body of the Volturno Plain (DAM, 2021). The Volturno Plain is a coastal plain of about 1340 km² constituted of fluvial, volcanic (i.e., pyroclastic) and marine sediments. It is surrounded by Mesozoic limestone mountains of the Southern Apennines (E), pyroclastic hills of the Phlegrean Fields (SW), adjacent plains (N and SE) and by the Thyrrenian sea (W). The Volturno River crosses the plain from NE to SW. Two main porous aquifers are present (Allocca et al. 2005; Corniello and Ducci 2014): a shallow phreatic one and a deep semi-confined (or confined) one, which are separated by a tuff layer of variable thickness. Groundwater chemistry reflects the geological characteristics of the study area, being influenced by volcanic edifices and related pyroclastic products and the closeness to carbonate rock formations. Calcium-bicarbonate facies is prevalent, with a gradual transition to alkaline type from the mountains towards the coast. In addition, ions concentration distributions highlighted the occurrence of seawater intrusion (Na^+, Cl^-) and anthropogenic contamination (K^+, NO_3^-, SO_4^{2-}) negatively affecting groundwater quality.

4.4.3 Methodologies

Methodologies encompass from the hydrogeological database implementation and field data collection to the statistical methods application.

4.4.4 Analytical methods

Base layers include elevation, hydrography, land cover and land use. Geological data include stratigraphies from more than 400 boreholes. Hydrogeological data include piezometric levels and more than 600 hydrochemical analyses (i.e., physico-chemical parameters, major and minor cations and anions, metals, organic compounds) from 370 wells and piezometers, spanning in the last 20 years. Hydrogeological data were collected by various entities (e.g., Regional Environmental Agency) for different purposes (e.g., monitoring campaigns, remediation activities) and were provided in extremely various formats. The realisation of the hydrogeological geo-database consisted in the collection and homogenisation of the information coming from different sources. Secondly, a quality check on the data was performed to identify errors, missing values and duplicate data. Errors and missing values were flagged, whereas duplicate data were removed from the database. Then, the basic, geological and hydrogeological data were organised in tables, vectorial and raster layers in a geographic information system (GIS) environment, according to the specific information contained in each single database (i.e., borehole stratigraphies, piezometric levels, hydrochemical data). Data formats were adjusted to respect the ISO (International Organization for Standardization) and the OGC (Open Geospatial Consortium) standards to make them accessible on a WebGIS platform.

4.4.5 Experimental methods

The monitoring activity begun in October 2022 continues, when a multiparametric probe was installed for the continuous measurement of the piezometric level and the parameters of electrolytic conductivity, temperature and salinity of the groundwater. The probe had been installed inside an unused well, located near the coastal area within an agricultural field managed by the "Le Terre di Don Peppe Diana" Cooperative, in Cancello ed Arnone (CE).

Periodic outings were carried out to verify the functioning of the instrument, maintenance and data collection. The monitoring activity is expected to be completed during 2024.

4.4.5.1 Modelling approaches

Long-term trends have been evaluated using Mann-Kendall trend test to show the spatial variability in ion concentrations in some part of the plain and in coastal areas. Moreover, a multivariate statistical analysis (i.e., factorial analysis, FA) is being performed to differentiate among the main hydrochemical processes occurring in the area. FA allows the handling of many geochemical and physical parameters (variables) measured in groundwater samples. The first results reveal different hydrogeochemical processes variably influencing the hydrochemical characteristics of the aquifers. The application of multivariate statistical analysis for the identification of factors determining the chemistry of groundwater used software freely available or available via university/department license for data preparation, analysis and visualization (Matlab, Python, SPSS , ArcGIS, QGIS).

4.4.6 Results

The hydrogeological geo-database summarises all the information collected in the Volturno Plain in the last two decades in a usable and interactive format. The exploration and interpretation of geological and hydrogeological data allow to reconstruct the geological and hydrogeological setting of the plain (Corniello and Ducci 2014), to delineate the groundwater body, to recognise the evolution of the hydrogeological characteristics over time, and to highlight missing information in the database. The hydrogeochemistry of the main aquifers reflects the geological characteristics of the study area, showing waters of calcium-bicarbonate type to sodium-bicarbonate type from the mountains to the seacoast, along the main groundwater flow direction. The high concentrations of As, F, Fe and Mn are strictly related to volcanic sediments and volcanic-related processes, especially in the south-eastern sector of the study area. The

spatial and temporal distribution of the main hydrochemical compounds (i.e., Cl^- and NO_3^-), combined with land use and land cover information, highlighted that the extensive presence of agricultural and livestock activities and urban and industrial settlements caused the worsening of groundwater quality in the last 20 years (Ducci et al. 2020).

Ions concentration distributions highlights the occurrence of seawater intrusion (Na^+, Cl^-) and anthropogenic contamination (K^+, NO_3^-, SO_4^{2-}) negatively affecting groundwater quality. Long-term trends (evaluated using Mann-Kendall trend test) show the variation in ion concentrations in some part of the plain and in coastal areas. Moreover, a multivariate statistical analysis (i.e., factorial analysis, FA) allows the differentiation among the main hydrochemical processes occurring in the area and the handling of many geochemical and physical parameters (variables) measured in groundwater samples. The first results reveal different hydrogeochemical processes variably influencing the hydrochemical characteristics of the aquifers.

4.4.7 Scientific products and dissemination

Del Gaudio E., Stevenazzi S., Onorati G., Ducci D. - Changes in geochemical and isotopic contents in groundwater before seismic events in Ischia Island (Italy). Chemosphere. 2023; 349:140935. https://doi.org/10.1016/j.chemosphere.2023.140935

Corniello A., Ducci D., Stellato L., Stevenazzi S. (corresponding author), Massaro L., Del Gaudio E. - Combining groundwater budget, hydrochemistry and environmental isotopes to identify the groundwater flow in carbonate aquifers located in Campania Region (Southern Italy). Submitted to Journal of Hydrology: Regional Studies on 18 December 2023.

Cocca D., Stevenazzi S., Ducci D., De Luca A.D., Lasagna M. - Spatio-temporal variability of groundwater hydrochemical features in different hydrogeological settings in Piedmont and Campania regions (Italy). Submitted to Acque Sotterranee - Italian Journal of Groundwater on 15 January 2024.

Ducci D., Stevenazzi S. – Nuevos aspectos cuali-cuantitativos del sistema hidrogeológico costero de la zona norte de Campania (sur de Italia). Revista del Museo de La Plata, 2023, Volumen 8, Suplemento Resúmenes: 15R-32R, DOI: 10.24215/25456377e018R, pp. 18R

6th Edition of Flowpath – National Meeting on Hydrogeology, Malta, 14th - 16th June 2023. Conference Proceedings Book. Sapiano M., Rusi S., Da Pelo S. (eds), pp. 130

Stevenazzi S., Zuffetti C., Camera C., Lucchelli A., Beretta G.P., Bersezio R., Masetti M. - Groundwater Resources Management in Mountainous Areas: A Regional Scale Approach in Lombardy Region (Northern Italy), pp. 16Di Matteo L., Ducci D., Allocca V., Calcaterra D., Carosi A., Cappelletti D.M., Cuello J., Cencetti C., Dell'Arciprete D., Di Martire D., Forte G., Gómez N., Guarracino L., Herrera F., Kruse E., Laurencena P., Lorenzoni M., Ortenzi S., Pendiuk J., Rodriguez Capítulo L., Sánchez Caro L., Stevenazzi S., Trovatto M.M., Valigi D., Villalba E., Carretero S. - Water Resource Management in Inland and Coastal Areas: Results Of Cooperation Between Italy and Argentina on Qualitative and Quantitative Issues of Groundwater and Surface Water Interactions, pp. 26

Stevenazzi S., Voudouris K., Ducci D., - Application of Multivariate Statistical Analysis for the Delineation of Groundwater Bodies: A Case Study in Campania Region (Southern Italy), pp. 65

Stevenazzi S., Massaro L., Corniello A., Ducci D. – Spatial and temporal patterns in the hydrogeochemistry of coastal aquifers in Campania Region (southern Italy). Congresso SIMP-SGI-AIV-SOGEI 2023. Società Geologica Italiana (ed.): Abstract book. pp. 1036, doi: https://doi.org/10.3301/ABSGI.2023.02.

Stevenazzi S., Voudouris K., Ducci D., - Application of multivariate statistical analysis as a support for the delineation of groundwater bodies: a case study in coastal plain areas of Campania Region (Southern Italy). IAH Congress 2023. Program and oral abstracts book, pp. 100.

Stevenazzi S., Massaro L., Ducci D. - Spatial distribution and temporal variation of groundwater physico-chemical features in coastal aquifers (Campania Region - Southern Italy). IAH Congress 2023. Poster list and abstracts book, pp. 33.

4.5 Direct measurements of hydrocarbon vapor emissions in sites subject to hydrocarbons' contamination by means of dynamic flux chambers: state of the art and experimental design (UNIPA)

(Contributors: Daniele Di Trapani, Gaspare Viviani, Alida Cosenza, Manuela Russo Tiesi)

4.5.1 Introduction

The contamination of environmental matrices represents nowadays a major concern due to the potential risk to humans, water, ecosystems or other receptors (Islam et al., 2017). Soil pollution due to petroleum hydrocarbons represents a major threat affecting soils globally mainly due by the mutagenic, carcinogenic, and toxic characteristics of such contaminants (Gidudu and Chirwa, 2020). Health Risk Analysis (HRA) procedure provides a quantitative assessment of the risk representing a useful tool to manage the risk. Indeed, depending on the severity of the risk as well as on current or planned use, the contaminated site might be subject to risk management measures, represented by remediation and/or security actions.

The Italian Legislation that regulates the reclamation of contaminated sites (Legislative Decree No. 152/2006) establishes the operational procedure aimed at verifying the actual level of contamination of a site and its eventual classification as "contaminated site" due to the potential risk to humans and/or water systems. The latter derives from the application a HRA carried out in agreement to the ASTM Standard (ASTM, 2000). The site investigation is of paramount importance since it implies the collection of prominent site-specific data and information about the contamination level, the pollutants migration pathways and the target exposure, thus enabling the build-up of an accurate Conceptual Site Model (CSM). This aspect is of particular concern in case of volatile organic compounds (VOCs) in soil of groundwater, such as petroleum hydrocarbons, since the vapor transport assumes a major role for the assessment of health risk for the selected targets, referring to inhalation pathway.

Traditionally, the applied "*fate&transport*" models are in general non-reactive diffusive, not considering the recurrence of reactive phenomena, related to biodegradation in the subsurface (Verginelli et al., 2018). As a consequence, the direct measurement of volatile compounds is assuming even more importance in the procedure for the assessment of site contamination, concerning the health risk analysis as well as the design of remediation procedure. Therefore, the aim of the activity is to carry out direct measurements of hydrocarbon vapor emissions in sites subject to hydrocarbons' contamination; these measurements will be used in the Health Risk Analysis (HRA) procedure, to highlight the beneficial use of direct gaseous measurements.

The direct measurement of volatile compounds is assuming even more importance in the procedure for the assessment of site contamination, concerning the health risk analysis as well as the design of remediation procedure. The aim of the proposed activity is to assess the influence of direct measurements in the health risk analysis carried out in a petroleum contaminated site. Specifically, the hydrocarbon vapours concentration in the subsurface soil porosity and the related emitted fluxes, measured through of a dynamic flux chamber, will be here considered. A thorough bibliographic review on the methods for the direct measurements of emitted flux from the subsurface soil has been carried out and the experimental equipment for field campaigns has been selected. It was decided to use the dynamic flux chamber, in agreement with the SNPA guidelines. The sampling grid, as well as the minimum number of monitoring points as been decided according to literature. The selection of a free-software, Risk-net 3.1 toolkit, has been done; this software enables to perform the comparison of measured data with those provided by applying a non-reactive diffusive model using the concentrations measured in the soil in terms of risk assessment, assessing eventual discrepancies with the expected outdoor concentrations obtained by using non-reactive diffusive models and highlighting potential model limitations, providing too precautionary and not realistic risk scenarios. Therefore, direct measurements might represent a cost-effective option to take into account the natural attenuation phenomena occurring in the subsurface, thus leading to more realistic Health Risk Assessment.

4.5.2 Case study description

The identification of experimental sites (even SNI) is under evaluation with Project Partners

4.5.3 Methodologies

The design of both monitoring and modelling experimental activities has been considered. According to the guidelines provided by SNPA (2018a,b,c,), it was established to carry out the direct measurement of hydrocarbon vapor concentrations in the subsurface soil porosity as well as the emitted fluxes through of a dynamic flux chamber, in soils subject to hydrocarbons' contamination. It was established to perform the monitoring activities also in contaminated Site of National Interest (SIN). It was decided that the field measurements are going to be repeated in seasonal experimental campaigns with the aim to optimize the measuring procedure. Moreover, it was established that the comparison of measured data with those provided by applying a non-reactive diffusive model is of prominent interest.

4.5.4 Analytical methods

The protocol to be developed in the activities has been deiced: In particular, it was decided to follow the procedure suggested by the guidelines SNPA on the design of field monitoring campaign as well as the proper use of field measurements in the risk analysis procedure (SNPA, 2018a,b,c). It was decided the number of sampling points to be monitored, which depends on the site set as case study. In more details, it was decided to split the overall area in grid cells (each grid cell = 50mx50 m = 2500 m^2), with a minimum number of three sampling points.

4.5.4.1 Experimental methods

The experimental apparatus for monitoring the emission flux has been decided and it consists in a dynamic flux chamber (Verginelli et al., 2018) (patented by Theolab s.r.l.). The chamber consists in a flat cylinder made in Teflon® with an inner diameter of 50 cm and height of 20 cm (Figure 7). Indeed, due to the expected low fluxes, it is not technically suitable the use of a static chamber, which might be rather convenient in a screening step. The flux chamber will be equipped with a tubular shaped windbreak positioned at the top of the box to minimize any interference due to wind (Saponaro et al., 2016). The inert gas carrier (high purity nitrogen) is introduced within the chamber through a multi-hole helical tubing, in order to guarantee complete mixing within the chamber. The pollutant concentration measured at the outlet of the experimental apparatus is equal to that inside the chamber; this value will enable to assess the flux emitted from the soil surface, as better outlined below.

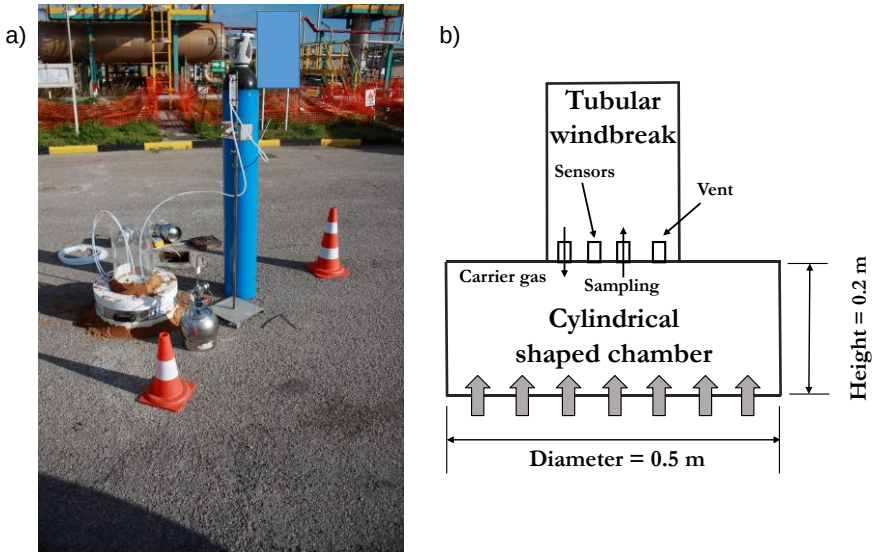

Figure 7. Panoramic view(a) and schematic layout (b) of the dynamic flux chamber that has been chosen for the monitoring field campaigns.

4.5.4.2 *Modelling approaches*

The mathematical activity has been derived from the work proposed by Verginelli et al. (2018). Based on the contaminant concentrations assessed inside the dynamic flux chambers, the flux of vapors emitted from the subsurface, $\Phi_{measured,fc}$, can be estimated using the equation derived from U.S.EPA (1986):

$$\emptyset_{measured,fc} = C_{fc} * \frac{Q_{fc}}{A_{fc}} \quad (1)$$

where C_{fc} represents the concentration of the contaminant measured inside the chamber, Q_{fc} the flowrate of the inert gas injected into the chambers and A_{fc}, the surface area of the chamber exposed to the soil.

In contrast, based on the concentrations of hydrocarbons measured in the soil and in groundwater, the vapor flux emitted from the subsurface is calculated through a diffusive model. Briefly, assuming no biodegradation in the subsurface, the flux of vapors emitted from the soil, $\Phi_{model,soil}$, can be calculated using the Fick's law:

$$Q_{model,soil} = C_{soil} * H * K_{ws} * \frac{D_{eff}}{L_{soil}} \quad (2)$$

with K_{ws} representing the water-soil partitioning coefficient:

$$K_{ws} = \frac{\rho_s}{\theta_w + \theta_a H + \theta_w K_d} \quad (3)$$

where Cs_{oil} is the concentration measured in the soil, H the dimensionless Henry's constant (i.e. the air–water partitioning coefficient), D_{eff} the effective diffusion coefficient in the vadose zone, L_{soil} the source depth in the vadose zone, ρs the soil bulk density, θ_w the moisture content in the soil, θ_a the air-filled porosity in the soil and K_d the soil to water partitioning coefficient.

Concerning the health risk analysis (HRA), the software selection was carried out. It was decided to use a free software, the Risk-net 3.1 toolkit, developed by RECONnet (Rete Nazionale sulla gestione e la Bonifica dei Siti Contaminati) which is in accordance with the Italian Regulation (Labianca et al., 2019). The procedure followed by the software agrees with the Risk Based Corrective Action (RBCA) procedure (ASTM, 2010); it enables the introduction data from direct measurements of soil gas and/or emission fluxes, thus allowing the comparison of the risk values obtained with or without direct measurements. The selectyed software Risk-net 3.1 toolkit enables to perform a HRA following both the traditional approach (i.e. applying a diffusive model) as well as starting with field measurements, thus comparing the different result and highlighting potential overestimation of health risk due to vapor inhalation by adopting the traditional approach.

4.5.5 Results

An in-depth bibliographic review was carried out to thoroughly understand the potential issues associated to direct measurements of hydrocarbon vapors in contaminated sites. In details, two main chamber-methods can be distinguished: static flux chambers and dynamic flux chambers (Hudson and Ayoko, 2008). The static method consists of closed containers inserted into the soil in which the vapors emitted at the soil surface are progressively accumulated (Gao and Yates, 1998). By measuring the concentration increase of vapors inside the chamber, it is possible to estimate the flux of vapors emitted (Pihlatie et al., 2013). A major issue for static chamber system is the headspace concentration increase during the sampling period, with the progressive accumulation of vapors inside the chamber that might modify the diffusion gradient that can lead to an underestimation of the flux (Heinemeyer and McNamara, 2011). The dynamic flux chamber method is similar to the static chambers one but in this case an inert gas is continuously introduced and an equivalent amount of the chamber gas is allowed to leave the chamber (Eklund, 1992). The emission rate of VOCs is then calculated based upon the surface area in contact with the soil, the applied flow rate and the measured gaseous concentration. In recent years dynamic flux chambers have been increasingly used for the assessment of pollutants 'emissions to the atmosphere from the subsurface.

In this context, the achieved results enable to highlight if a traditional approach used in the assessment of health risk based on contaminant concentrations measured in soil or groundwater might led to unrealistic or to an

overestimation of the human target exposure, due to the use of simple diffusive models that do not take into account biodegradation of hydrocarbon vapors.

4.6 Assessment of reactive transport processes in porous systems (POLIMI)

(Contributors: Chiara Recalcati, Laura Ceresa, Alberto Guadagnini, Enrico Zio, Davide Marzi)

4.6.1 Introduction

Accurate assessment of reactive transport processes taking place in porous systems across various spatial scales is key in a variety of environmental and industrial scenarios of pressing concern. Accurate modeling of these phenomena is generally constrained by various sources of uncertainties. These arise from our lack of knowledge of mechanistic processes driving reaction kinetics that, in turn, induce spatial (and temporal) variations of physical and/or chemical properties of the system. Breaking such knowledge barrier and developing robust theoretical frameworks embedding prediction uncertainties is critical to provide efficient strategies to mitigate environmental and health risks associated with underground water bodies. In this context, we pursue the two research lines described in the following.

Research Line 1 investigates mechanistic nanoscale processes driving reaction kinetics. Recent studies show that the action of such small-scale phenomena yields highly heterogeneous spatial distributions of surface reactivity. Such a remarkable spatial variability, in turn, casts serious doubts about the possibility to exhaustively represent material fluxes taking place across fluid-rock interfaces solely through average rate values (Lüttge et al., 2013; Fischer et al., 2012). We rely on state-of-the-art Atomic Force Microscopy (AFM) imaging to investigate the effect of these processes on the heterogeneity of reaction rates. We aim to establish a reliable experimental protocol that allows employing AFM to collect high-quality big datasets of absolute material fluxes across the surface of a crystal subject to reaction under continuous flow conditions. These are then modeled upon relying on a stochastic approach that embeds the presence of diverse kinetic modes jointly driving the reaction. We start by focusing on a system characterized by a low degree of chemical complexity entailing the dissolution of a calcite crystal in deionized water. Calcite is selected because of its significance in environmental contexts as part of the carbon cycle (Bouissonnié et al., 2018) and as a key potential sink for toxic compounds (see, e.g., Renard et al., 2018; 2019; Heberling et al., 2014; Julia et al., 2023; Guren et al., 2020), in line with the main drivers underlying the overall concept of RETURN.

Research Line 2 is geared towards developing rigorous mathematical formulations enabling quantification of estimation and predictive uncertainty in the context of geochemical modeling of complex reaction networks underpinning geochemical processes typical of Emerging Organic Contaminants (EOCs). These are compounds spanning from, e.g., nanomaterials, food additives and industrial chemicals, to personal care products and pharmaceuticals characterized by a persistent and bioactive nature. Despite their small concentration, their presence in surface and subsurface water bodies poses serious threats for the environment and for human life. Their behavior is not yet fully understood nor regulated (Dulio & Slobodnik, 2009). Among them, we tackle the fate of the pharmaceutical Diclofenac (Dcf) in groundwater under biotic denitrifying redox conditions. We propose a comprehensive hydro-geochemical model that is capable to interpret reactive transport dynamics of Dcf and major ions/compounds involved in its speciation in water, encompassing uncertainty sources. We embed our formulation in a stochastic framework by relying upon inverse modeling grounded on a maximum likelihood (ML) approach assisted by modern global sensitivity analysis (GSA).

4.6.2 Methodologies

In the context of *Research Line 1* we develop novel (*i*) experimental and (*ii*) modeling workflows, respectively illustrated in Section 4.6.2.1 and Section 4.6.2.2. Modeling strategies developed in the context of *Research Line 2* are detailed in Section 4.6.2.2 and applied to a selected experiment (Silver et al., 2016; 2018; denoted as *Column A experiment* therein).

4.6.2.1 Experimental methods

The designed experimental setting is depicted in Figure 9.A. The mineral sample is prepared by cleaving a calcite crystal of Iceland Spar (Mexico) along the {104} plane to obtain fragments of thickness ~1 mm. A

metallic mask (of thickness 40±1 nm) is directly fabricated on the sample surface through a combination of optical lithography and electron beam evaporation (Barri et al., 2020). The sample is glued onto a glass slide secured on a support plate that is magnetically attached to the AFM. A fluid cell (of volume V~2 mL) open to air is mounted on the support plate and sealed with a Viton O-ring. The cell is connected to a high precision syringe pump (Cetoni, Nemesys S) equipped with two independent modules. The sample is fluxed with a continuous flow rate Q = 10 μLs^{-1} for the entire duration of the experiment. Such a flow rate ensures that the chemical conditions in the fluid remain stable, while also guaranteeing that any imaging distortions associated with the flow field are limited (Recalcati et al., 2023). Dissolution of the sample is induced at ambient conditions (i.e., pressure $p = p_{atm}$ and temperature $T = 22$°C) by using deionized water. Under such chemical settings, calcite dissolves by forming rhombohedral mono- and multilayer etch pits (see, e.g., Teng, 2004; Bouissonnié et al., 2018). The former are shallow ephemeral surface features that can nucleate randomly on crystal terraces or at point defects and have a depth of a single crystal layer (Harstad & Stipp, 2007). These features arise in the presence of screw dislocations and spread laterally and vertically, removing several layers of the lattice. We design AFM scanning (Keysight 5500 apparatus) in tapping mode by employing silicon tips with an aluminum coated cantilever (Nanosensors, PPP-NCHR, k=42 Nm^{-1}). Imaging is performed over a surface of 20×20 μm^2 area across a 1024×1024 horizontal grid (pixel size 19.5 nm), comprising a portion covered by the mask ≥ 40% of the total scanned area. Having at our disposal such reference level is key to obtain absolute values of reaction rates as it allows one to remove spurious contributions associated with scanning artifacts and/or vertical drifts of the piezoelectric scanner while keeping the actual retreat. Indeed, AFM data are generally affected by artifacts, including bowing effects induced by the scanning mechanism (Ricci & Braga, 2004; Marinello et al., 2010) and thus require a preliminary processing phase of the acquired signals. This is performed by removing the underlying background, $B(\mathbf{x}, t)$. The latter is modeled as a first order polynomial and is evaluated making use of the topographic data corresponding to the non-reacted portion of the surface. The ensuing estimated surface is then subtracted from the measured topography, $z_{meas}(\mathbf{x}, t)$, yielding the actual crystal topography, $z(\mathbf{x}, t)$ [m], i.e., $z(\mathbf{x}, t) = z_{meas}(\mathbf{x}, t) - B(\mathbf{x}, t)$. Spatial distributions of rates, $R(\mathbf{x}, t)$ [mmol m^{-2} s^{-1}], are then evaluated as

$$R(\mathbf{x}, t) = \frac{z(\mathbf{x},t) - z(\mathbf{x},t+\Delta t)}{\Delta t \cdot V_m}, \quad (1)$$

where Δt [s] is the temporal interval between two measurements and $V_m = 36.93 \cdot 10^{-9}$ m^3 mmol^{-1} is calcite molar volume. All experiments are performed at Polimi in the Interdepartmental Laboratory Solid-Liquid Interface Nanomicroscopy and Spectroscopy Lab (SoLINano-Σ Lab).

4.6.2.2 Modelling approaches

Research Line 1

We account for the occurrence of various mechanisms yielding diverse rate modes upon relying on a Gaussian Mixture (GMIX) modeling framework (Siena et al., 2023). We view dissolution rates as multi-modal random fields, i.e.,

$$R(\mathbf{x}, t) = \sum_{m=1}^{M} I_m(\mathbf{x}, t) \cdot R_m(\mathbf{x}, t), \quad (2)$$

where $I_m(\mathbf{x}, t)$ is an indicator random variable independent of the m^{th} component/mode of the mixture, $R_m(\mathbf{x}, t)$. The indicator $I_m(\mathbf{x}, t)$ allows to differentiate between different spatial regions within the observation window. Each of these regions is associated with a distinct kinetic process and is described through a Bernoulli distribution with mean $E\{I_m(\mathbf{x}, t)\} = p_m(t)$. The latter corresponds to the relative proportion of $I_m(\mathbf{x}, t)$ across the domain. We focus on a bimodal Gaussian field, i.e., $M = 2$ in Eq. (2) and $R_m(\mathbf{x}, t) \sim N(\mu_m, \sigma_m^2)$, with $m = A, B$, μ_m and σ_m^2 being the mean and the variance of the m^{th} mode of the mixture. Setting $E\{I_A(\mathbf{x}, t)\} = p$, the probability density function (PDF) of R is

$$f_R(r) = \frac{p}{\sqrt{2\pi}\sigma_A} e^{-\frac{(r-\mu_A)^2}{2\sigma_A^2}} + \frac{(1-p)}{\sqrt{2\pi}\sigma_B} e^{-\frac{(r-\mu_B)^2}{2\sigma_B^2}}. \quad (3)$$

Estimation of model parameters embedded in Eq. (3) relies on a custom sequential algorithm based on a Bayesian classifier with minimum-error-rate (see, e.g., Duda, 2001; James et al., 2013).

Research Line 2

We propose a reactive transport model coupling a set of advective-dispersive-reactive mass transfer processes taking place under single-phase, steady-state flow regime. Our geochemical modeling framework is implemented in the PHREEQC environment (Parkhurst & Appelo, 2013). Problem position is set to resemble experimental conditions in Silver et al. (2018). Figure 8.A provides a schematic illustration of our modeling setup. The simulation of the overall reactive process is split into subsequent (in time) sub-simulations across which the advective velocity, u, can be considered as constant (see Figure 8.B). Each sub-simulation features a specific temporal discretization scheme selected to ensure that the algorithm advects one pore volume of water across two neighboring cells in exactly one time step, as prescribed in PHREEQC environment. Initial concentrations of each $i = 1, \dots, N_{SP}$ species (N_{SP} being the total number of chemical species), $C_{0,i}$, are set to match temporal changes that these undergo during the experiment (see as an example the variation in time of the initial concentration of NO_3^- depicted in Figure 8.C). The system is considered as initially filled with a background water solution having identical aqueous speciation as the infilling fluid at the beginning of the experiment. We assign fixed concentration-type and no-flux boundary conditions at column inlet and outlet, respectively. The modeling framework yields the following one-dimensional (1D) formulation of the advective-dispersive-reactive transport equation (ADRE):

$$\begin{cases} \frac{\partial C_i(x,t)}{dt} = -u(t)\frac{\partial C_i(x,t)}{dx} + \alpha u(t)\frac{\partial^2 C_i(x,t)}{dx^2} + \frac{R_i}{\phi} \\ C_i(x, t=0) = C_{0,i}(t=0) \\ C_i(x=0) = C_{0,i}(t) \\ \frac{\partial C_i(x=L,t)}{dx} = 0 \end{cases} \quad (4)$$

Here, R_i represents the change in concentration C_i of species i at time t and location x due to the occurrence of chemical reactions; parameters $\alpha = 3.5$ cm and $\phi = 28.5\%$ denote the average system dispersivity and effective porosity, respectively (Silver et al., 2016).

The chemical reactions implemented in our model are schematized in Figure 8.D. These include (*i*) a sequence of microbially-mediated redox transformations (modeled according to multiple Monod kinetics; see Appelo & Postma, 2005), (*ii*) dissolution/precipitation and (*iii*) dissociation/(aqueous) complexation equilibria, and (*iv*) Dcf acid adsorption on the organic carbon fraction of soil (modeled as a surface complexation process). Modeling of the kinetics included in such a complex reaction network entails $N_P = 22$ uncertain parameters (listed in Table 1). These are estimated upon calibrating the model through a stochastic inverse modeling algorithm set in the PEST suite (Doherty, 2015) and resting on a Maximum Likelihood approach. The latter entails minimization of the negative log-likelihood (Carrera & Neuman, 1986). Under certain assumptions, this is tantamount to minimizing the summation of weighted square residuals between model prediction of the concentration of chemical species i, C_{ijk}, and observation, C^*_{ijk}, evaluate at fixed sampling ports, $j = 1, \dots, N_{PORTS}$ (see Figure 8.A) and times, $k = 1, \dots, N_{i,T}$ (N_{PORTS} and $N_{i,T}$ being the number of sampling ports and times, respectively). We rely on a set of assumptions that are commonly considered in hydrogeology (see, e.g., Dell'Oca et al., 2023; Ceresa et al., 2023), i.e., (*i*) the variance associated with prior measurement errors is the same for all data, (*ii*) such errors are mutually independent, and (*iii*) uncertain model parameters and observations are distributed according to a multi-Gaussian probability density function. Hence, our objective function reads as:

$$\begin{cases} \varphi = \sum_{i=1}^{N_{SP}} \varphi_i, \\ \varphi_i = \sum_{j=1}^{N_{PORTS}} \sum_{k=1}^{N_{i,T}} w_{ijk} \left(\frac{C_i(x_j,t_{ik}) - C_i^*(x_j,t_{ik})}{C^{*(max)}_{ij}} \right), \\ C^{*(max)}_{ij} = \max_{k=1,\dots,N_{i,T}} \left(C_i^*(x_j,t_{ik}), \dots, C_i^*(x_j,t_{iN_{i,T}}) \right), \\ w_{ijk} = \frac{1}{N_i} \forall j,k, \end{cases} \quad (5)$$

where w_{ijk} is the weight of the residuals and is here selected as the inverse of the total number of data available for each compound/species, N_i. Such a stochastic calibration technique allows one to quantify the uncertainty associated with estimated model parameters upon relying on the post-estimation covariance matrix, $\mathbf{\Sigma}$ (see Carrera & Neuman, 1986).

Table 1 – Uncertain parameters embedded in our model formulation.

Parameter		U.M.	Pertaining process
Maximum nitrate rate constant	r_{max1}	s^{-1}	reduction of dissolved nitrate, NO_3^-, to dissolved nitrite, NO_2^-
Methanol half saturation constant	$K_{half1}^{CH_4O}$	mol L^{-1}	
Nitrate half saturation constant	$K_{half1}^{NO_3^-}$	mol L^{-1}	
Maximum nitrite rate constant	r_{max2}	s^{-1}	reduction of dissolved nitrite, NO_2^-, to dissolved elemental nitrogen, N_2
Methanol half saturation constant	$K_{half2}^{CH_4O}$	mol L^{-1}	
Nitrite half saturation constant	$K_{half2}^{NO_2^-}$	mol L^{-1}	
Reaction inhibition constant	K_{inh2}	mol L^{-1}	
Maximum iron oxy-hydroxide rate constant	r_{max3}	s^{-1}	reduction of amorphous (solid) dissolved iron oxy-hydroxide, $Fe(OH)_3$ to dissolved iron, Fe^{2+}
Methanol half saturation constant	$K_{half3}^{CH_4O}$	mol L^{-1}	
Iron oxy-hydroxide half saturation constant	$K_{half3}^{Fe(OH)_3}$	mol L^{-1}	
Reaction inhibition constant	K_{inh3}	mol L^{-1}	
Maximum pyrolusite rate constant	r_{max4}	s^{-1}	reduction of pyrolusite, MnO_2, to dissolved manganese, Mn^{2+}
Methanol half saturation constant	$K_{half4}^{CH_4O}$	mol L^{-1}	
pyrolusite half saturation constant	$K_{half4}^{MnO_2}$	mol L^{-1}	
Reaction inhibition constant	K_{inh4}	mol L^{-1}	
Maximum sulphate reduction rate constant	r_{max5}	s^{-1}	reduction of dissolved sulphate, SO_4^{2-}, to dissolved hydrogen sulphide, H_2S
Methanol half saturation constant	$K_{half5}^{CH_4O}$	mol L^{-1}	
Sulphate half saturation constant	$K_{half5}^{SO_4^{2-}}$	mol L^{-1}	
Reaction inhibition constant	K_{inh5}	mol L^{-1}	
Reaction rate constant (associated with 2nd order kinetic law)	k_6	L mol^{-1} s^{-1}	Iron sulphide, FeS, precipitation from dissolved Fe^{2+} and HS^-
Reaction rate constant (associated with 1st order kinetic law)	k_7	s^{-1}	Rhodocrosite, $MnCO_3$, precipitation from Mn^{2+} and CO_3^{2-}
Organic carbon-water partition coefficient of diclofenac acid, **HDcf**	$\widetilde{K}_{OC}^{HDfc}$	L mol^{-1}	Diclofenac, Dfc, adsorption of the organic carbon fraction in soil

Additionally, we implement a parameter-oriented global sensitivity analysis (GSA) to investigate the possible occurrence of uncertain model parameters associated with negligible levels of influence on model outputs, Δ (i.e., φ and φ_i in Eq.(5)). This rests on evaluation of the $AMAE^{(\Delta)}$ metrics (Dell'Oca et al., 2017) of the selected quantities for each uncertain parameter of the proposed hydro-geochemical model, i.e.:

$$AMAE^{(\Delta)} = \frac{|\mathbb{E}[\Delta|\theta] - \mathbb{E}[\Delta]|}{|\mathbb{E}[\Delta]|}. \quad (6)$$

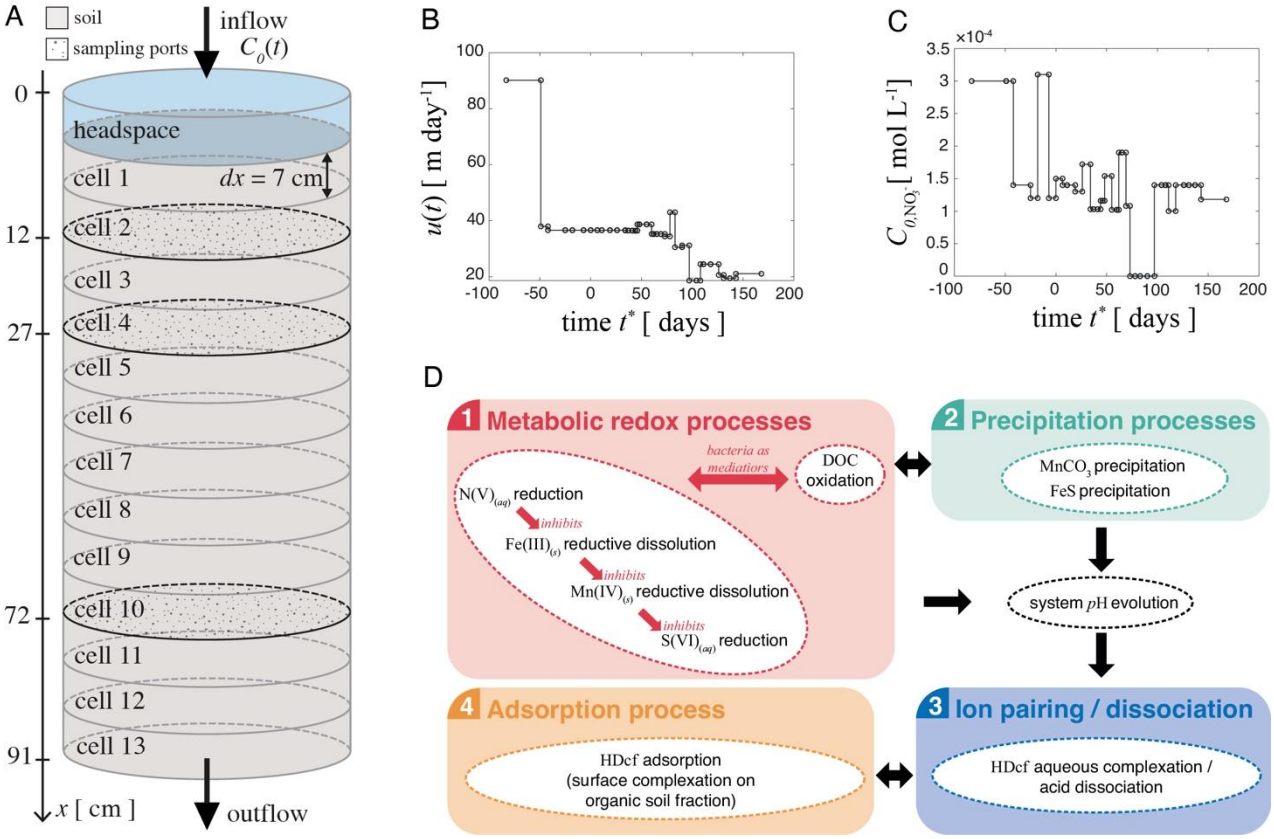

Figure 8: (A) Schematic representation of the model setup in the context of *Research Line 2*. Measured (B) advective velocity, u, and (C) initial concentration of nitrate, C_{0,NO_3^-}, against time, t^*, monitored during *Column A experiment* by Silver et al. (2016; 2018). (D) Schematic representation of key chemical processes embedded in our modeling framework.

4.6.3 Results

Research line 1

Figure 9.B depicts an exemplary snapshot of calcite surface topography (scaled with respect to the inert layer) measured at t = 34 min from the beginning of the dissolution experiment. The reaction is dominated by vertical deepening and horizontal spreading of two multilayer etch. These exhibit different temporal behaviors, yielding a complex surface pattern. The deep etch pit on the left of Figure 9.B (MP-L) evolves by forming trains of steps. The latter behavior is consistent with a description based on the stepwave model described by Lasaga & Lüttge (2001; 2003). These authors conceptualize material fluxes from the surface as governed by spreading of steps originating from screw dislocations, which then travel across the crystal surface. In contrast, spreading of the etch pit on the right (MP-R) of Figure 9.B remains limited and its flat bottom acts as a nucleation site for other shallow etch pits. Merging of stepwaves radiated from MP-L and MP-R leads to a complex pattern of steep rhombohedral steps in the region comprised between these two main features. Figure 9.C depicts an exemplary spatial distribution of $R(\mathbf{x}, t)$ evaluated though Eq.(1). This exhibits traits that are consistent with recent experimental findings associated with a different context and documented by Fischer & Lüttge (2018) who rely on VSI and observe a pulsating dissolution mechanism of stepwaves originating from etch pits on a Zinc oxide surface.

Evaluation and analysis of sample probability densities is critical to obtain information about the probability of occurrence of ranges of rate values across the mineral surface. Unlike standard approaches grounded on the assessment of an average rate (i.e., a constant rate value), which is then considered as a unique value characterizing the bulk surface retreat, relying on a stochastic approach enables one to capture the richness of information governing the complexity underlying the evolution of mineral surface reactivity (Lüttge et al., 2013; Fischer et al., 2012). Figure 9.D depicts the sample PDF associated with the spatial map of R illustrated in Figure 9.C. The average value of rates (black circle in Figure 9.D) aligns with data reported

for similar chemical conditions by Bouissonnié et al. (2018) and Arvidson et al. (2003) (denoted by green and light blue circles, respectively). Consistency between our experimental results and literature data imbues us with confidence on the reliability of the designed experimental protocol to evaluate absolute reaction rate data.

Sample distributions exhibit pronounced multi-modal traits leading to long right tails. Similar features have been observed for calcite and other carbonate minerals through AFM analyses (Emmanuel, 2014; Siena et al., 2021; 2023) as well as at larger spatial scales typical of Vertical Scanning Interferometry (Bibi et al., 2018; Bollermann & Fischer, 2020), Digital Holographic Microscopy (DHM) (Brand et al., 2017), or X-ray microtomography (Noiriel et al., 2018). Modeling results based on Eq. (3) juxtaposed to sample PDF are depicted in Figure 9.D, documenting the remarkable ability of our theoretical framework to capture the essential elements of the experimental observations. Vertical red and blue lines depict component means, μ_m, along with corresponding intervals of semi-width equal to one standard deviation, σ_m $(m = A, B)$. These identify ranges for low and high rates that are fully consistent with those obtained by Brand et al. (2017) which are associated with identical chemical conditions to those considered here, even as acquired at a larger spatial scale via DHM observations of a polished calcite surface (pink rectangles in Figure 9.D).

Our analysis documents that the proposed modeling framework can encapsulate coexisting and/or competing behaviors of surface features governing the reaction. As such, it responds to the critical need to include small scale processes in the interpretation of sample rate PDFs to provide a comprehensive description of reaction kinetics. Having at our disposal a rich dataset of absolute rates enables us to (*i*) accurately assess the detailed features (including tailing and extreme values) of the ensuing PDFs and (*ii*) characterize the statistical traits of each component of the PDF through mode deconvolution.

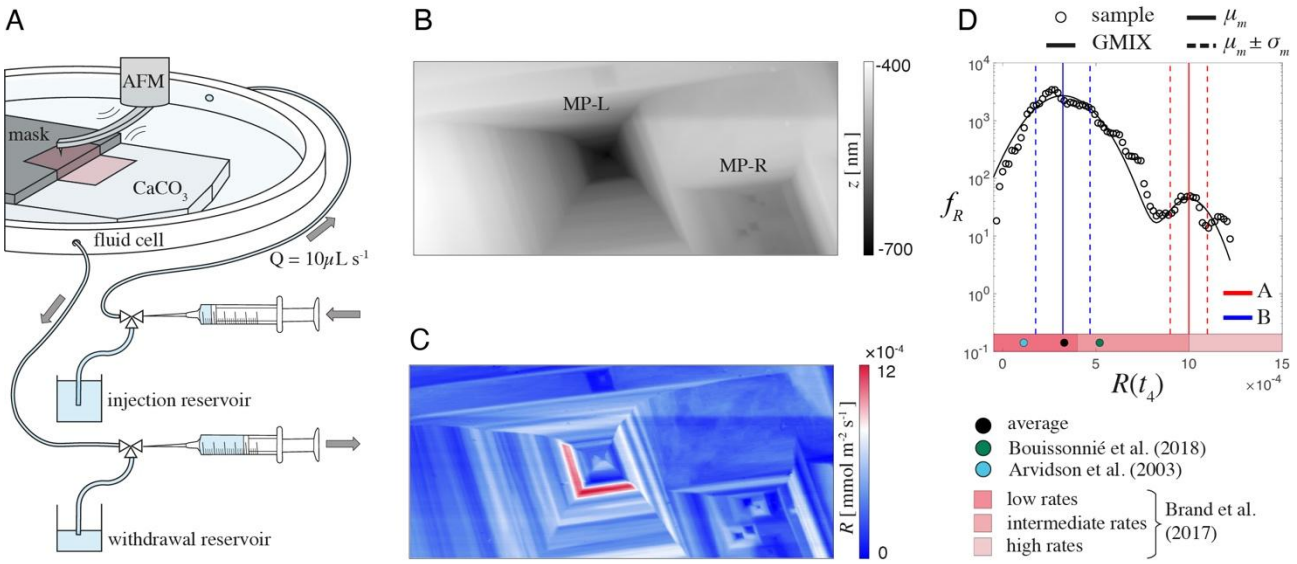

Figure 9: (A) Schematic depiction of the experimental setup designed in the context of *Research Line 1*. (B) Exemplary topography image collected at observation time $t = 34$ min from the beginning of the dissolution experiment. (C) Spatial heterogeneity of absolute dissolution rate, $R(\mathbf{x}, t)$, at $t = 34$ min. (D) Sample PDF and GMIX model (Eq.(3)) associated with $R(\mathbf{x}, t = 34$ min). Vertical red and blue lines depict component means, μ_m, along with the intervals of semi-width corresponding to one standard deviation, σ_m $(m = A, B)$. Average value (black circle) and literature data (green and light blue circles) are also depicted. Pink rectangles delineate intervals of low, medium, and high rates as evaluated by Brand et al. (2017).

Research line 2

We perform a preliminary optimization of the set of uncertain parameters embedded in our modeling framework (see Eq.(4) and Table 1) upon relying on Eq.(5). This reveals marked difficulties in the simultaneous estimation of all uncertain parameters due to (*i*) data paucity and (*ii*) evidences of cross-correlation of some parameters. As often experienced in a wide variety of hydro-geological scenarios entailing a large number of uncertain parameters with an insufficient level of empirical information, also our first optimization run is associated with an extremely large condition number ($\sim 10^{11}$) of the Fisher

information matrix. The latter corresponds to the inverse of the post-estimation covariance matrix, i.e., $\mathbf{F} = \mathbf{\Sigma}^{-1}$. If its condition number exceeds the $5 \cdot 10^7$ threshold, reliability of calibration results is doubtful (Doherty, 2015). Analysis of the entries of the post-estimation covariance matrix also documents the emergence of cross-correlation between some model parameters. Aiming to improve the accuracy of model calibration, we then consider investigation of the results of the parameter-oriented GSA prior to model inversion. This enables one to (*i*) identify parameters that have a negligible effect on model output to exclude them from the estimation stage and (*ii*) assess the effect of uncertain parameters on geochemical processes encompassed in the modeling framework. Relying on such analysis is also instrumental to unravel the geochemical nature underpinning cross-correlations between parameters and, in turn, to possibly reduce model complexity in favor of calibration accuracy.

We start by applying the GSA to the overall model (i.e., the calibration cost function φ in Eq. (5)). We then apply the GSA on model outputs associated with species i (i.e., φ_i in Eq. (5)) that are demarcated as relevant by the former sensitivity analysis. The resulting values of $AMAE^{(\varphi)}$ indexes are depicted in Figure 10.A. These show that most influential parameters (corresponding to orange bars in Figure 10.A) are related to the formulation of redox reaction rates associated with biotic reduction of nitrate, nitrite, iron, and manganese (i.e., those included in the red rectangle in Figure 10.D). Otherwise, uncertain parameters appearing in the kinetic law associated with the remaining processes (gray bars in Figure 10.A) exhibit a lower degree of influence on the overall calibration cost function. In the following, we discuss the results obtained for $AMAE^{(\varphi_{\mathrm{NO_3^-}})}$ (depicted in Figure 10.B) as an illustrative example of the GSA performed on model outputs associated with relevant single species. Figure 10.B suggests that parameters directly involved in the mathematical formulation of $\mathrm{NO_3^-}$ reduction (i.e., r_{max1} , $K_{half1}^{\mathrm{CH_4O}}$ and $K_{half1}^{\mathrm{NO_3^-}}$) are critical to determine the partial contribution to the total cost function ascribed to nitrate concentrations residuals. However, also uncertain parameters embedded in the mathematical formulation of $\mathrm{SO_4^{2-}}$ reduction (i.e., r_{max5} and $K_{half5}^{\mathrm{CH_4O}}$), affect the variability of $\varphi_{\mathrm{NO_3^-}}$. This is probably due to the fact that, among all redox-sensitive species competing in our system to undergo reduction sustained by the degradation of available organic carbon, sulphate is the unique compound that is present at large concentrations in pore water (being one of the major anions in water speciation). Otherwise, other chemical species such as, e.g., dissolved iron and manganese, occur at much lower ranges of concentration in the considered soil-water system, thus playing a less significant role in affecting the rate of $\mathrm{CH_4O}$ oxidation. These findings, together with those related to results of the GSA applied to nitrite, iron, and manganese reduction, lead us to conclude that some parameters are inherently cross-correlated, as they reflect interactions among geochemical processes taking place in the system.

In light of the GSA outcomes, we choose to limit our model calibration to the estimation of the sole 10 uncertain parameters featuring a high impact on model output (i.e., those associated with orange bars in Figure 10.A) and to set the remaining ones at constant values. Given the impossibility to separate the estimation of some parameters based on available data, we start a preliminary analysis resting on a set of simplifications of the mathematical modeling of the associated kinetic laws. This entails reformulating some processes as functions of *equivalent uncertain parameters*, i.e., combinations (such as ratios and/or products) of uncertain parameters whose action on the model output cannot be decoupled. The reduced dimensionality (i.e., reduced number of parameters) characterizing this second simplified model formulation enables us to (*i*) reduce the condition number of **F** and, in turn, (*ii*) obtain an accurate calibration of the model yielding results that are in good agreement with sample data. As an example, Figure 10.C depicts results for Dfc concentration evaluated at three different locations juxtaposed to experimental data collected by Silver et al. (2018).

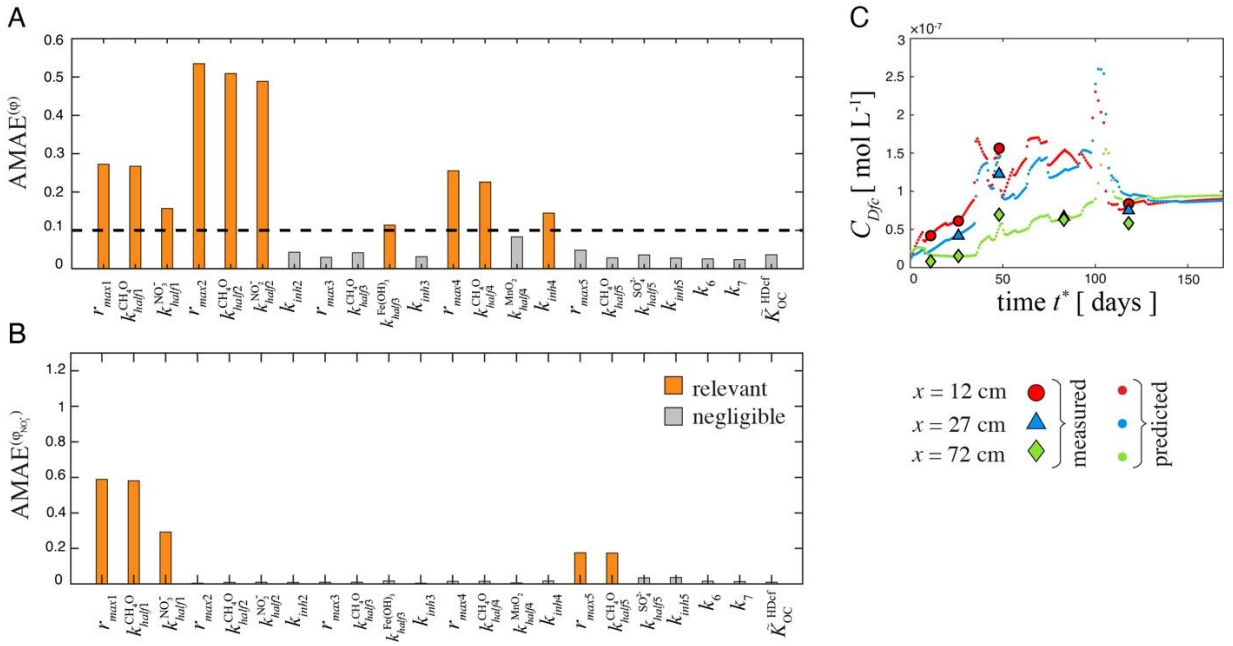

Figure 10: Values of $AMAE$ sensitivity indices for (A) overall model cost function, φ, and (B) cost function contribution associated with nitrate reduction, $\varphi_{NO_3^-}$, versus uncertain parameters embedded in our modeling framework. (C) Predicted evolution of the concentration of Diclofenac at $x = 12$ cm, $x = 27$, and $x = 72$ cm (corresponding to the three sampling ports in *Column A experiment* by Silver et al. (2016; 2018)). Measured concentration values are also depicted.

4.6.4 Scientific products and dissemination

Research papers (under review or in preparation)

Recalcati, C., Siena, M., Bollani, M., Riva, M., & Guadagnini, A. (2024). Stochastic assessment of dissolution at fluid-mineral interfaces. *Under review*.

Ceresa, L., Riva, M., & Guadagnini, A. (2024). Stochastic inverse modeling of diclofenac dynamics in porous media. *In preparation*.

Conference presentations (submitted abstract)

Ceresa, L., Riva, M., & Guadagnini, A. (2024, June). Stochastic Inverse Modeling of Diclofenac Dynamics in Groundwater. *Submitted to GeoEnv2024 Conference*.

Recalcati, C., Siena, M., Bollani, M., Riva, M., & Guadagnini, A. (2024, April). Investigation of mineral dissolution kinetics through Atomic Force Microscopy. *Submitted to EGU2024 General Assembly Conference.*

Conference presentations

Ceresa, L., Guadagnini, A., Riva, M., & Porta, G. M. (2023, July). Modeling the fate of Diclofenac in soil-water systems. In *Goldschmidt 2023 Conference*.

Recalcati, C., Siena, M., Riva, M., & Guadagnini, A. (2023, July). Stochastic modeling of calcite dissolution rates from microscale observations. In *Goldschmidt 2023 Conference*.

Recalcati, C., Siena, M., Riva, M., & Guadagnini, A. (2023, May). Direct nanoscale investigation of calcite dissolution kinetics. In *Interpore 2023 Conference*.

4.7 A method for calibrating the Transient Storage Model from the early and late-time behavior of breakthrough curves (UNIPD)

(Contributors: Andrea Bottacin Busolin, Andrea Marion)

4.7.1 Introduction

Tracer tests have been widely used for characterizing the fate and transport of solutes in streams and rivers. The tests are typically conducted by injecting a tracer upstream and observing the evolution of the tracer concentration at one or more sections downstream. Reach-averaged transport parameters are then estimated by fitting a one-dimensional model to the observed breakthrough curves (BTCs). Several models have been proposed to represent solute transport in open-channel flows, among which the Transient Storage Model (TSM) proposed by Bencala and Walters [1983] has found widespread application to both field and laboratory data. The TSM is based on the classical advection-dispersion equation with the addition of a first-order mass transfer term representing storage in finite volume zones. The model has been shown to provide reasonably good approximations of tracer test breakthrough curves [Bencala and Walters, 1983; Mulholland et al., 1997; Valett et al., 1996], although better fits can be obtained by assuming two storage components with different detention time [Briggs et al., 2009; Bottacin-Busolin et al., 2011]. Several works have analyzed the capability of the TSM to consistently represent the dynamics of solute retention in streams [Marion et al., 2003; Zaramella et al., 2003; Marion et al, 2005].

In the present work, a graphical approach was developed for estimating the parameters of the TSM. This was done by deriving specific approximations for the initial rising phase and the final decreasing phase of the concentration curves, and by identifying the conditions which allow separate determination of transport and storage parameters from the BTCs. The applicability of the newly derived approximations for deriving the parameters of the TSM from the independent fit of the rising and decreasing parts of a BTC was demonstrated with numerical tests and with an application to experimental data. Results show that the graphical estimation of transient storage parameters and longitudinal dispersion coefficient is feasible if two conditions are satisfied: first, when longitudinal dispersion and transient storage do not produce an overlapping effect on the rising limb of the BTC and, secondly, when the condition of approximation of the decreasing limb as an exponential function is satisfied. However, a specific condition applies to the distance from the injection point for the validity of these approximations, which represents a limit of separability between longitudinal dispersion and first-order mass transfer in immobile domains. When this condition is not satisfied, longitudinal dispersion and transient storage become two undistinguishable mixing processes that cannot be uniquely separated by fitting the model to a tracer BTC. The condition also provides a lower limit for the timescales of solute retention that can be inversely modelled from a tracer experiment. This limit should therefore be considered in the design of tracer tests and subsequent analyses to provide meaningful parameter estimates and identify sources of uncertainty.

4.7.2 Case study description

The applicability of the proposed approach was demonstrated with experimental data from a field tracer test. The data were taken from the experimental work of Bottacin-Busolin et al. [2011] conducted on the Desturo canal, an irrigation channel located in Northern Italy.

The Desturo canal is a small 5.6 km-long drainage canal which is part of the drainage basin of the Venice Lagoon in Northern Italy. The canal is located just outside of an urban settlement and is used for irrigation purposes. It is affected by pollution due to distributed inputs of fertilizers used in agricultural activity, but the main sources of pollution are due to input of water from a waste-water treatment plant of the nearby Monselice village and to inputs of non-treated water during rain periods from urban drainage systems. The total length of the canal reach considered in this study is 3300 m and has almost uniform characteristics with few channel bends. The channel cross section is trapezoidal, with flood plains and natural banks. The canal has only thin vegetation on the banks, with virtually no masts and bushes. The sediment bed is made of a sandy–silty material, and at the time of the tests there were algae, submerged vegetation, and pieces of marsh reeds.

4.7.3 Methodologies

4.7.3.1 Modelling approaches

In the TSM model the river channel is conceptually divided into two mutually interacting domains: (1) a main flow channel with cross-sectional area A, in which the bulk flow occurs, and (2) a storage domain of finite cross-sectional area A_S adjacent to the main channel. The cross-sectional average concentration of solute is assumed to be homogeneous in the main channel and in the storage area, and the corresponding concentrations are denoted by C_W and C_S, respectively. The coupled differential equations governing the evolution of the concentration along the river are:

$$\frac{\partial C_W}{\partial t} + U\frac{\partial C_W}{\partial x} - D_W\frac{\partial^2 C_W}{\partial x^2} = -\frac{A_S}{A}\frac{\partial C_S}{\partial t} \quad (1)$$

$$\frac{\partial C_S}{\partial t} = \alpha\frac{A}{A_S}(C_W - C_S) \quad (2)$$

where D_W is the longitudinal dispersion coefficient in the bulk flow and α is the exchange rate of solute at the storage zone-bulk flow interface. The model above implies an exponential residence time distribution (RTD) in the dead zones, $\varphi(t) = (1/T_D)e^{-\frac{t}{T_D}}$, with $T_D = \frac{1}{\alpha}\frac{A_S}{A}$ as the mean residence time in the storage zone, and can be shown to be equivalent to other more general residence time formulations under the assumption of a single storage domain with exponential RTD [Marion et al., 2008]. Following Davis et al. [2000], the solution to Equations 1 and 2 for an instantaneous injection of mass M of conservative tracer at $x = 0$ and at $t = 0$ can be written as:

$$C_W(x,t) = C_T(x,t)\mathrm{e}^{-\alpha t} + e^{-\frac{t}{T_D}}\int_0^t C_T(x,t)e^{-\frac{t}{T_D}}\sqrt{\frac{\alpha}{T_D}}e^{-\alpha\tau}\sqrt{\frac{\tau}{t-\tau}}\ I_1\left[2\sqrt{\frac{\alpha}{T_D}}\sqrt{\tau(t-\tau)}\right]d\tau \quad (3)$$

where I_1 is the first-order modified Bessel function of the first kind, and

$$C_T(x,t) = \frac{M}{2A\sqrt{\pi D_W t}}e^{-\frac{(x-Ut)^2}{4D_W t}} \quad (4)$$

is the solution to Equation 1 when transient storage is disregarded. In the alternative formulation proposed by Davis et al. [2000], referred to as the Aggregated Dead Zone (ADZ) model, the longitudinal dispersion term in Equation 1 is dropped, $D_W = 0$, and the corresponding solution for an instantaneous mass injection at time $t = 0$ is:

$$C_W(x,t) = \frac{M}{AU}\delta\left(t-\frac{x}{U}\right)\ e^{-\alpha t} + \frac{M}{AU}H\left(t-\frac{x}{U}\right)e^{-\frac{t-\frac{x}{U}}{T_D}}\mathrm{e}^{-\frac{\alpha x}{u}}\sqrt{\frac{\alpha}{T_D}\left(\frac{\frac{x}{U}}{t-\frac{x}{U}}\right)}\ I_1\left[2\sqrt{\frac{\alpha}{T_D}}\sqrt{\frac{x}{U\left(t-\frac{x}{U}\right)}}\right] \quad (5)$$

where $\delta(t)$ is the delta Dirac function and $H(t)$ is the Heaviside function.

Approximation of the rising part of the BTC

Equation 4 implies that $C_T e^{-\alpha t}$ is the portion of mass M that never entered the storage domain. As a first approximation this term describes the Rising part of a BTC, observed at a section X following an instantaneous injection of mass M at $x = 0$:

$$C_R^{\delta}(x,t) = \frac{M}{2A\sqrt{\pi D_W t}}e^{-\frac{(x-Ut)^2}{4D_W t}}\ e^{-\alpha t} \quad (6)$$

An approximation for this part of the curve in case of a step injection of tracer of duration T_S at $x = 0$ can be derived from the convolution of C_W, expressed by Equation 3, with the concentration at the boundary.

Neglecting the contribution of the second term of Equation 3, the approximating expression for the rising part of the BTC is found as

$$C_R^H(x,t) = \left\{\frac{QC_T(x,t)}{M}\right\} * \{C_0\ [H(t) - H(t-T_S)]\} = \int_0^{T_S} \frac{C_0 Q}{M} C_T(x, t-\tau)d\tau$$
$$= \frac{QC_0}{A}\ \frac{e^{-\frac{\alpha x}{U^3}(U^2-\alpha D)}}{2U}\left[\mathrm{erf}\left(\frac{U^3 t - U^2 x + 2\alpha D x}{2\sqrt{U^3 D x}}\right) - \mathrm{erf}\left(\frac{2\alpha D x - U^2(UT_S + x - Ut)}{2\sqrt{U^3 D x}}\right)\right] \quad (7)$$

where C_R^H is the approximation of the rising part of the BTC, and $H(t)$ is the Heaviside function. The error function, $\mathrm{erf}(y)$, can be approximated near $y = 0$ by its McLaurin series:

$$\mathrm{erf}(y) = \frac{2}{\sqrt{\pi}} \sum_{n=0}^{\infty} \frac{(-1)^n y^{2n+1}}{(2n+1)n!} \quad (8)$$

By limiting the series expansion to the first two terms and substituting into Equation 7 under the frozen cloud approximation used by Chatwin [1971], a linear approximation is found for the rising limb in the case of a finite-length step injection at $x = 0$:

$$C_R^H(X,t) = mt + q \quad (9)$$

where

$$m = \frac{C_0 U e^{-\alpha \frac{X}{U}}}{\sqrt{4\pi D_W \frac{X}{U}}} \quad (10)$$

and

$$q = \frac{C_0 e^{-\alpha \frac{X}{U}}}{2}\left[1 - \frac{2}{\sqrt{\pi}}\left(\frac{X}{\sqrt{4D_W \frac{X}{U}}}\right)\right]. \quad (11)$$

Equation 9 represents the rising limb of a BTC at section X resulting from a step concentration C_0 at $x = 0$ from $t = 0$ to the time $t = T_S$. This approximation applies around the point $t = X/U$, where $C_W(X,t) \simeq C_0/2$.

Approximation of the decreasing part of the BTC

Equation 5 can be used to obtain an approximation for the decreasing limb $C_D^{\delta}(X,t)$ of a BTC following an instantaneous injection of mass M at $x = 0$. After some time from the concentration peak, the decreasing limb is represented by Equation 5, provided that the term describing the concentration front in Equation 4, given by $C_T(x,t)e^{-\alpha t}$, is negligible for $t \gg 0$. The modified Bessel function of first order and first kind can be approximated by a linear equation $I_1(x) \simeq x/2$ in the range $0 < x < 1$ [38], or more accurately by the series [Abramowitz and Stegun, 1972]:

$$I_\nu(x) \simeq \frac{x^\nu}{\nu\Gamma(\nu)}\left[1 + \frac{x^2}{4(\nu+1)} + \frac{x^4}{32(\nu+1)(\nu+2)} + \frac{x^8}{6144\sum_{n=1}^{4}(\nu+n)}\right] \quad (12)$$

valid for $x \leq 12$ or $x \leq \nu$. Using a second order approximation, thus limiting the series expansion of I_1 to the second term of Equation 12, the expression of I_1 in Equation 5 can be approximated as follows:

$$I_1\left[2\sqrt{\frac{\alpha}{T_D}}\sqrt{\frac{x}{U}\left(t - \frac{x}{U}\right)}\right] \simeq \sqrt{\frac{\alpha}{T_D}}\sqrt{\frac{x}{u}\left(t - \frac{x}{U}\right)} + \frac{1}{2}\left(\frac{\alpha}{T_D}\right)^{3/2}\left(\frac{x}{U}\right)^{3/2}\left(t - \frac{x}{U}\right)^{3/2} \quad (13)$$

Equation 13 is valid for $x/U < t < x/U + T_D/(2\alpha x/U)$. By substituting Equation 13 into Equation 5, the following approximating expression for the decreasing part of the BTC is obtained:

$$C_D^{\delta}(x,t) = \frac{M\alpha\frac{x}{U}}{T_D Q} e^{-\alpha\frac{x}{U}} e^{-\frac{t-\frac{x}{U}}{T_D}} \left[1 + \frac{\alpha}{2T_D}\frac{x}{U}\left(t - \frac{x}{U}\right)\right] \quad (14)$$

For $x/U < t < x/U + T_D/(2\alpha x/U)$, another approximation can be derived,

$$\left[1 + \frac{\alpha}{2T_D}\frac{x}{U}\left(t - \frac{x}{U}\right)\right] \simeq e^{\frac{\alpha}{2T_D}x/U\left(t-\frac{x}{U}\right)} \quad (15)$$

which leads to the final approximated expression for Equation 14:

$$C_D^{\delta}(x,t) = ae^{n(x)t} \quad (16)$$

where:

$$a(x) = \frac{M\alpha\frac{x}{U}}{T_D Q} e^{-\frac{\alpha}{2T_D}\left(\frac{x}{U}\right)^2 - \frac{\alpha T_D - 1}{T_D}\frac{x}{U}} \quad (17)$$

and:

$$n(x) = \frac{\alpha}{2T_D}\frac{x}{U} - \frac{1}{T_D} \quad (18)$$

Equation 5 describes the behavior of the decreasing limb of a BTC generated by an instantaneous injection of tracer when the effect of the mass transfer into the dead zones is much greater than the effect of longitudinal dispersion at late times. For a step injection of tracer at $x = 0$, the expression for the decreasing limb must be suitably modified. In this case, the concentration at the injection section can be expressed as $C_0[H(t) - H(t - T_S)]$. If a solute mass M is injected at $x = 0$ with a constant rate over the time T_S starting at $t = 0$, the approximated expression of the decreasing limb can be found from the convolution integral,

$$C_D^{H}(x,t) = \int_0^{T_S} \frac{QC_0}{M} a e^{n(t-\tau)} d\tau = \left\{\frac{QC_{DL}^{\delta}(x,t)}{M}\right\} * \{C_0[H(t) - H(t - T_S)]\}. \quad (19)$$

The solution to Equation 19 is again an exponential function:

$$C_D^{H}(x,t) = be^{n(x)t} \quad (20)$$

where:

$$b(x) = \left\{-e^{-\left(\frac{\alpha}{2T_D}\frac{x}{U} - \frac{1}{T_D}\right)\left(T_S + \frac{x}{U}\right)} + e^{-\left(\frac{\alpha}{2T_D}\frac{x}{U} - \frac{1}{T_D}\right)x/U}\right\} \frac{2C_0\alpha}{\alpha\frac{x}{U} - 2}\frac{x}{U} e^{-\alpha\frac{x}{U}} \quad (21)$$

To determine the limit of applicability of the proposed approximation it is convenient to introduce the non-dimensional time, defined as $t^* = t/(X/U)$, and the non-dimensional longitudinal coordinate, $x^* = x/X$, where X is a characteristic length. Using these non-dimensional quantities, Equation 13 can be written for a fixed cross section $x = X$ as:

$$I_1\left[2\sqrt{\frac{\alpha}{T_D}\frac{X}{U}\sqrt{(t^* - 1)}}\right] \simeq \sqrt{\frac{\alpha}{T_D}\frac{X}{U}\sqrt{(t^* - 1)}} + \frac{1}{2}\left(\frac{\alpha}{T_D}\right)^{3/2}\left(\frac{X}{U}\right)^3 (t^* - 1)^{3/2} \quad (22)$$

valid for $1 < t^* < t_{LIM}^*$, where t_{LIM}^* is a non-dimensional parameter defined as:

$$t_{LIM}^* = 1 + \frac{T_D U^2}{2\alpha X^2} \quad (23)$$

The parameter t_{LIM}^* represents the upper time limit for which Equation 22 approximates the modified Bessel function. The lower limit, $t^* = 1$, corresponds to the non-dimensional advective time $t_{AD}^* = t_{AD}/(X/U)$, where $t_{AD} = X/U$.

4.7.4 Results

The analytical approximations presented above were first validated numerically and then applied to experimental data as a demonstration of the proposed graphical parameter estimation approach.

Numerical validation

The validity of the approximations derived above was tested by simulating BTCs with the TSM using prescribed values of A, A_S, D_W, and α and by graphically comparing the simulated BTCs with the approximations expressed by Equations 10, 11, 18 and 21. We assume the flow discharge $Q = 0.25$ m^3 s^{-1}, stream width $b = 5.0$, and depth $d = 0.4$ m. The dispersion coefficient is estimated using Fischer's formula, $D_W = 0.011U^2b^2/(U^*d) = 0.735$ m^{2}s^{-1} [40], where the shear velocity is $U^* = \sqrt{gdj} = 0.037$ m s^{-1} and j is the energy slope under the assumption of uniform flow and for a Manning's coefficient $n = 0.05$ m$^{-1/3}$s^{-1}. The model output is generated using a single compartment TSM with storage area $A_S = 0.1$ m^2, and exchange rate $\alpha = 10^{-4}$ s^{-1} at three cross-sections located at $X_1 = 500$ m, $X_2 = 1000$ m and $X_3 = 1500$ m from the injection point. The boundary condition at $x = 0$ is a constant concentration C_0 injection of a solute mass M $= 192$ g applied for a period $T_S = 480$ s starting at $t = 0$ s.

Figure 11 shows the dimensionless output concentration $C^*(X,t) = C_W(X,t)/\ C_p(X,t_p)$, where $C_p(X,t_p)$ is the peak concentration at time t_p, at the three chosen sections in both semi-log and linear scales. The approximations for the rising and the decreasing parts of the BTC are plotted according to Equations 9 and 20 in linear and semi-log scale respectively, where the parameters m, q, b and n are evaluated from Equations 10, 11, 18 and 21 with the same parameters used for the TSM. The values of A, A_S, D_W, α, m, q, b, n and t^*_{LIM} are reported in Table 2 for each section.

Application to field tracer data

The applicability of the proposed approximations was demonstrated with experimental data from a field tracer experiment from the work of Bottacin-Busolin et al. [2011]. The studied reach is divided into two sections located at $X_1 = 262$ and $X_2 = 567$ m respectively from the injection point. The plateau injection of a mass of tracer $M = 3240$ g is $T_S = 1470$ s long and the flow discharge is $Q = 0.045$ m^3 s^{-1}. At both section X_1 and X_2 a linear and an exponential trendline are applied to the leading and the decreasing limb respectively, considering the portion of data in the leading and decreasing limbs which maximize the coefficient of determination R^2. The trend lines are reported in Figure 12, which shows the observed concentrations and the trendlines in linear scale for the rising limb (panels a and b) and semi-log scale for the decreasing limb (panels c and d). The trendlines provide the values of m and q of the approximation for the rising part, $C^*_R(t) = mt + q$, and the values of b and n of the exponential approximation for the decreasing part of the curve, $C^*_D(t) = be^{nt}$. The unknown transport parameters A, A_S, D_W and α are obtained by solving Equations 10, 11, 18 and 21 as a system of equations. The resulting transport parameters and t^*_{LIM} are reported in the first two lines of Table 3.

To check the quality of the fit, the obtained transport parameters are then used for generating a BTC with the TSM. A comparison between the simulated BTCs (dashed-dot blue line) and the observed data (circles) is reported in Figure 12 in linear (panel a and b) and semi-log scales (panel c and d). The observed BTCs are then numerically fitted with the TSM by using differential evolution as an optimization algorithm. The computed parameters A, A_S, D_W and α for the optimized fitted BTC are reported in Table 3 for comparison with the parameters obtained using the proposed approximations. The best fitting BTCs are reported in Figure 12 (dashed red line).

4.7.4.1 Discussion

The results of the numerical validation presented in Figure 11 show that the accuracy of the graphical estimation of the transient storage parameters and longitudinal dispersion coefficient varies at the three sections, suggesting that the method can be applied only when certain conditions are satisfied. In particular, it can be noted that the approximations are good at the first section X_1, but start to deviate from the rising and decreasing parts of the BTC at X_2, further downstream of the injection point. At the furthest section X_3 the decreasing part of the BTC is not well fitted by the approximations expressed by equations 19 and 21. This means that the BTC does not behave exponentially at late time as expressed by Equation 20. Similarly, the rising part is no longer described by Equation 9. There are two reasons for this behavior: first, the term $C_T = C_W e^{-\alpha t}$ in Equation 4 becomes negligible at longer times and for higher exchange rates α; secondly, at late times Equation 13 is not a good approximation of the Bessel function. At late times and at large distances from the injection point, the contribution of transient storage to the mixing process becomes more important than longitudinal dispersion, therefore transient storage and longitudinal dispersion become two overlapping processes. This means that the rising limb of the curve no longer represents the sole effect of

longitudinal dispersion. At the same time, the decreasing limb of the curve does not behave as an exponential function anymore and therefore does not decrease exponentially as predicted by Equation 13. The dimensionless upper time limit of validity for Equation 22, t^*_{LIM}, can represent a numerical index for identifying the conditions of applicability of the approximation method proposed in this work. For sections $X_1 = 500$ m, $X_2 = 1000$ m, and $X_3 = 1500$ m, the values of t^*_{LIM} are 1.40, 1.10, 1.04, respectively. These values suggest that transient storage does not produce an exponential behavior of the decreasing limb when the upper time limit of validity of Equation 22, t^*_{LIM}, is close to 1. Although there is no definite value for t^*_{LIM}, the results suggest that, in general, the exponential behavior associated with the transient storage term is not well distinguishable from the longitudinal dispersion effect when $t^*_{LIM} \ll 1.1$.

Application of the approach to the experimental data confirms the validity of the approach for $t^*_{LIM} > 1.1$ Results show that when the approximations for the leading and decreasing limbs of the observed BTCs are applied, the BTC generated by the TSM with the graphically estimated parameters for section $X_1 = 262$ m (dashed-dotted lines in Figure 12 a and c) well fit the observed data. At this section, the upper nondimensional time limit of validity for Equation 22 is $t^*_{LIM} = 1.33 > 1.10$. The set of parameters obtained with the proposed graphical method can provide a good first approximation of the parameters obtained by the numerically calibrated parameters. Their relative percentage errors are: +15% for D_W, +1% for A, -21% for A_S, and -29% for α. For the mean residence time in the storage zone, T_D, evaluated according to Equation 3, the relative error between the model generated BTCs with the graphically and numerically estimated parameters is +10%. Conversely, at section $X_2 = 567$ m, where $t^*_{LIM} = 1.02$, the graphical approximation does not lead to a well-fitted BTC (dashed-dotted lines in Figure 12 b and a), as the time of the peak concentration is poorly caught and both the leading and decreasing limbs are not well approximated. At this section, model calibration based on a global optimization algorithm yields a very different set of parameters, as shown in Table 3. The relative errors between the graphically obtained and the numerically calibrated parameters are -89% for D_W, -9.5% for A, -0% for A_S, -230% for α and -67% for T_D.

The graphical method presented in this work thus provides a simple preliminary way for evaluating transient storage parameters in field experiments, and can be considered reliable when $t^*_{LIM} > 1.1$. The dimensionless parameter t^*_{LIM} provides useful hints on whether longitudinal dispersion and transient storage are two distinguishable processes or not. The empirical rule $t^*_{LIM} > 1.1$ can also be expressed in terms of the advective time t_{AD} according to the following relations:

$$t^*_{LIM} = 1 + \frac{T_D U^2}{2\alpha X^2} = 1 + \frac{A_s}{2\alpha^2 A}\frac{1}{t^2_{AD}} > 1.1 \tag{24}$$

$$t_{AD} < \sqrt{\frac{1}{0.1}\frac{A_s}{2A\alpha^2}} \tag{25}$$

which are more likely satisfied when the BTC is observed at relatively short distances from the injection.

Table 2. TSM parameters A, A_S, D_W, α used for the concentration curves in Figure 11 and coefficients m, q, b, n of the proposed approximations at the three sections X_i.

Section	Distance	D_W	A	A_s	α	t^*_{LIM}	n	b	m	q
	(m)	($m^2 s^{-1}$)	(m^2)	(m^2)	(s^{-1})	(-)	(s^{-1})	(-)	(s^{-1})	(-)
X_1	500					1.400	-1.75e-03	4.63e+01	2.04e-03	-4.32
X_2	1000	0.735	2.00	1.0e-01	1.0e-04	1.100	-1.50e-03	2.22e+03	1.63e-03	-7.27
X_3	1500					1.044	-1.25e-03	2.00+04	1.31e-03	-8.96

Table 3. Coefficients m, q, b, n for the trendlines in Figure 12; TSM parameters A, A_S, D_W, α obtained from the trendline approximations ("Approx.") and from numerical fit ("Optim.") of the BTCs; estimated values of t^*_{LIM} for each section and calibration method.

Section	Distance	Fit	n	b	m	q	D_W	A	A_s	α	t^*_{LIM}
	(m)		(s-1)	(-)	(s-1)	(-)	(m2 s-1)	(m2)	(m2)	(s-1)	(-)
X_1	262	Approx.	-2.11e-03	98.5	2.21e-03	-2.278	0.279	0.202	2.93e-02	4.00e-04	1.33
		Optim.	-	-	-	-	0.243	0.200	3.72e-02	5.65e-04	1.21
X_2	567	Approx.	-1.80e-03	4252.9	8.86e-04	-2.582	0.090	0.244	1.86e-02	4.55e-04	1.02
		Optim.	-	-	-	-	0.535	0.270	1.86e-02	1.37e-04	1.16

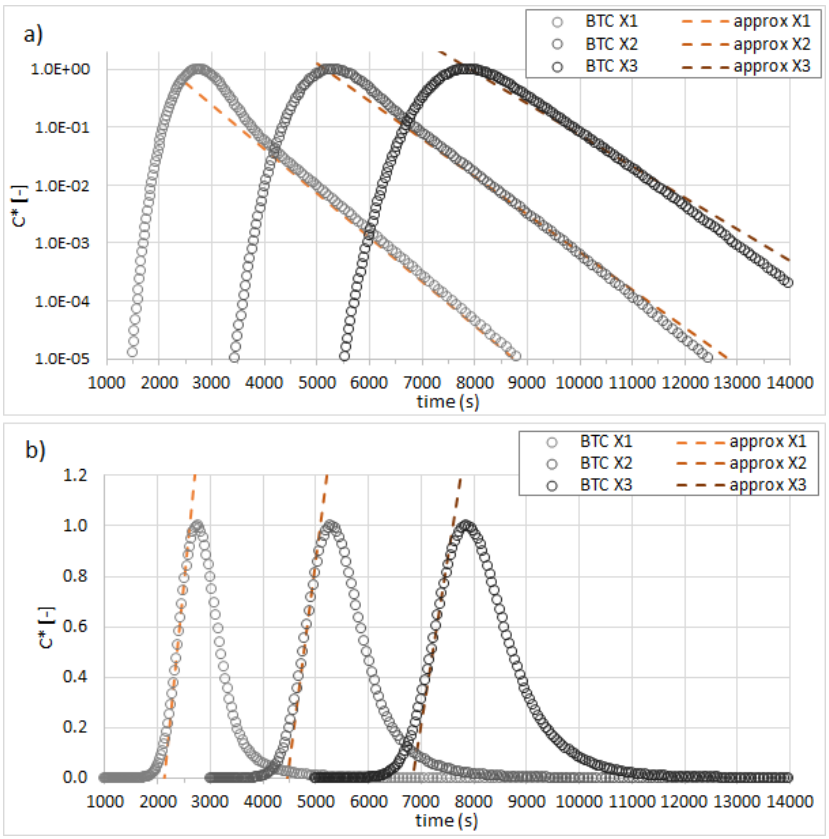

Figure 11. BTCs generated with the TSM at $X_1 = 500$ m, $X_2 = 1000$ m and $X_3 = 1500$ m and approximations for (a) the decreasing part in semi-log scale and (b) the rising part of the BTCs in linear scale.

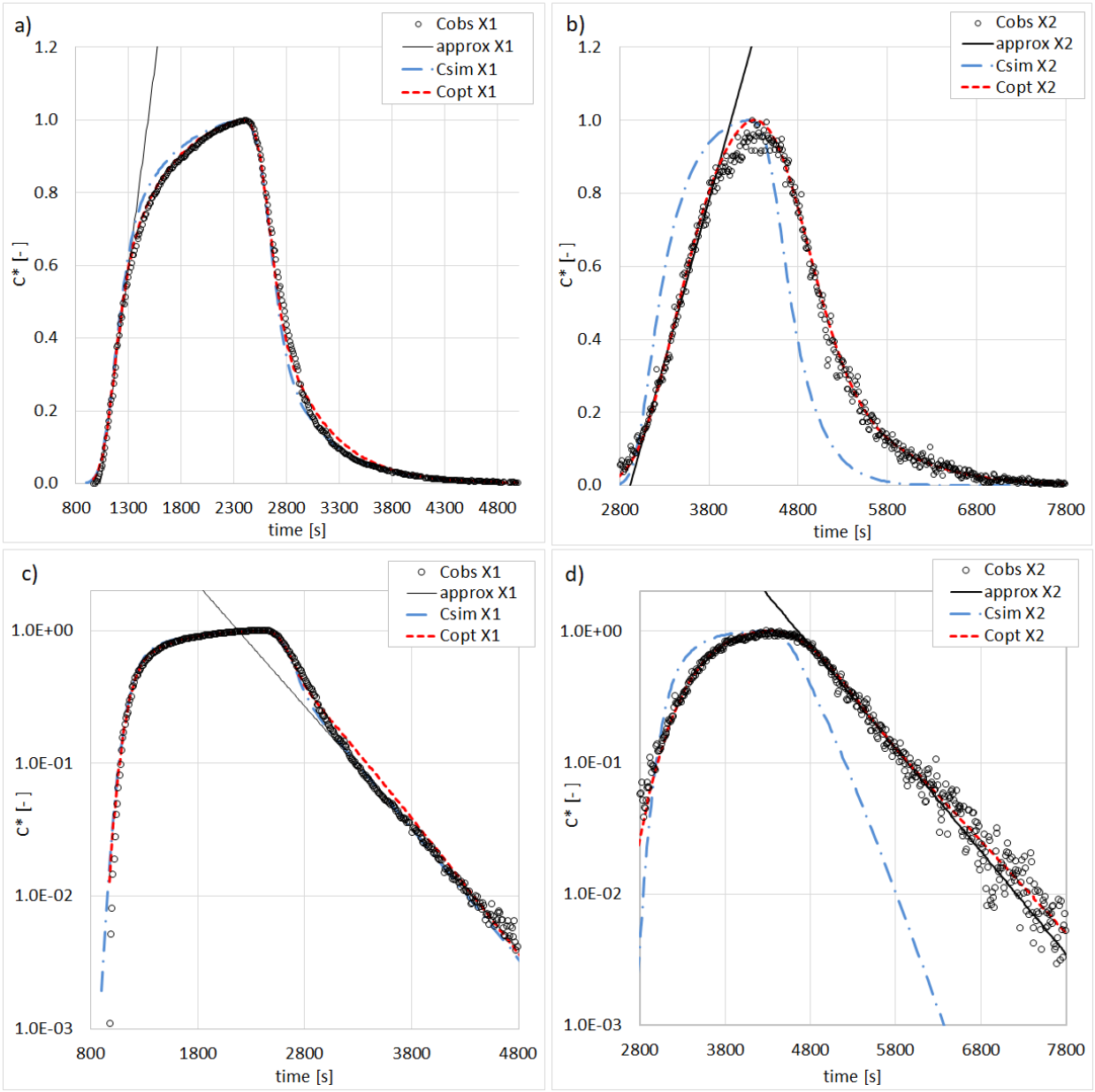

Figure 12. Observed concentration data ("Cobs", circles), trendlines based on the proposed approximations (solid black lines), simulated BTCs from the approximations ("Csim", dashed-dot blue lines), and numerically fitted BTCs generated with the TSM ("Copt", dashed red lines) for section X1 (panels a and c) and section X2 (panels b and d). Panel a) and b) show the proposed approximation for the rising part of the BTC. Panel c) and d) are in semi-log scale and show the proposed approximation for the decreasing part of the BTC.

4.7.5 Scientific products and dissemination

Dallan, E., Bottacin-Busolin, A., Zaramella, M., Marion, A (2023). A Method for calibrating the Transient Storage Model from the early and late-time behavior of breakthrough curves. Water, 15, 979. https://doi.org/10.3390/w15050979

4.8 Integrated Stochastic Modeling of Sustainable Urban Water Systems: Managing Hazards from Cross-Contaminations (POLIMI)

(Contributors: Manuela Antonelli, Beatrice Cantoni)

4.8.1 Introduction

Integrated Urban Water Systems (IUWS) are vital components of modern cities, serving as conduits for safe water supply, wastewater management, and environmental protection. A transition towards a "water-wise city" is prompted by factors such as increasing population density, heightened water scarcity, and the imperative for alternative water sources, notably reclaimed water, used for industrial and agricultural purposes. Concurrently, rising rainfall intensities increase the occurrence of Combined Sewer Overflows (CSOs) with direct release of mixed wastewater and stormwater from the sewer to the environment, while fluctuations in industrial activities and precipitation levels create additional complexities in water management. Furthermore, the demand for clean water bodies for recreational purposes adds another layer of significance to urban water quality management.

Within this intricate urban water landscape, managing water quality emerges as a pivotal challenge, given the diverse array of pollutant sources, pathways, and receptors. Contaminants in urban areas derive from various origins, including industrial and municipal wastewater treatment plants discharges, urban runoff from streets and construction sites. Consequently, rivers, canals, and groundwater reservoirs serve as storage, interconnection and transport for an assortment of contaminants, posing threats to aquatic ecosystems and the environment. Moreover, in case of direct and indirect reuse of reclaimed wastewater in agriculture, contaminants potentially present in the irrigation water can be transferred into the edible crops whose consumption can pose a risk for human health. The complex interplay of physical factors and chemical reactions further complicates the fate and transport of pollutants within urban water systems, making water quality assessment a multifaceted endeavor. Moreover, all these aspects are further complicated for emerging contaminants (such as pharmaceuticals (PHARMS), pesticides (PESTS), Per- and Poly-fluoroalkyl Substances (PFAS), alkylphenols, phthalates, Heavy Metals (HMs), Polycyclic Aromatic Hydrocarbons (PAHs)) due to the knowledge gaps and high uncertainties related to their occurrence, release, fate and effects.

In response to these challenges, there is a pressing need for innovative methodologies to effectively monitor contaminants in urban water systems. Overall, this research contributes to the advancement of methodologies for contaminants monitoring in urban water systems by addressing these key challenges and proposing innovative approaches. In fact, by improving our understanding of the environmental risks posed by CSOs, evaluating the impacts of transitioning to water-wise cities, and enhancing methodologies for assessing reclaimed wastewater reuse, this study aims to provide valuable insights and tools for enhancing the sustainability and resilience of urban water management practices. This goal is achieved by developing integrated tools to evaluate what are the main sources of different contaminants in urban areas to support decision-makers in the identification of the streams, contaminants and frequencies for an optimal planning of monitoring campaigns in the urban system. This holistic evaluation provides decision-support for sustainable water management strategies, identifying critical sources and points along the waterway in current and future scenarios.

4.8.2 Case study description

The analyzed system boundaries were defined, to consider all the compartments involved in the process, from sources to the final endpoint, whether it is the environment or human health. A schematic overview of a water-wise city with several water sources, fluxes, uses and reuses is reported in Figure 13.

4.8.3 Methodologies

All the analyzed hazards have a common methodology as a basis to support decisions on the monitoring: a risk-based approach is used to identify the main sources and exposure routes of micropollutants for the environment and human health.

4.8.3.1 Modelling approaches

The developed procedure for risk assessment includes several steps. As for the exposure assessment step, the exposure routes to be investigated are identified within the system to consider all the main exposure sources. Then, micropollutants concentration data were retrieved from literature for each compartment. Additional modeling of micropollutants fate is used to predict micropollutants concentration at the endpoint knowing the concentrations in each source and modelling the hydraulic system. Then, in the hazard assessment step, the toxicological characterization for each micropollutant was taken from the literature. Finally, exposure and hazard assessment steps are combined in the risk characterization step, to quantitatively estimate environmental or human health risk for micropollutants in different sources.

The Risk Quotient (RQ) for environmental risk has been calculated as follows:

$$RQ_{i,j} = \frac{C_{i,j}}{TL_j} \cdot \frac{V_i \cdot n_i}{Q_R \cdot t} \quad \text{Eq. 1}$$

where i is the discharge source (e.g. CSO, WWTP by-pass (BP), WWTP effluent (EFF), Groundwater Heat Pumps (GHP)); j is one micropollutant that may cause chronic toxicity; $C_{i,j}$ is the distribution of the concentration of the j micropollutant in the discharge i; V_i is the distribution of the annual volume released in the river by each discharge, n_i is the number of structures per discharge; Q_R is the distribution of the river annual average flowrate; t is the reference time (1 year); TL_j is the Toxic Level for the j micropollutant, that is the minimum value between the Annual Average Environmental Quality Standards (AA-EQS), set by the European Parliament in 2013, and the lowest Chronic Predicted No-Effect Concentration ($PNEC_{chronic}$), collected from the NORMAN database.

The Benchmark Quotient (BQ) for human health risk has been calculated as follows:

$$BQ_{i,j} = \frac{C_{k,j} \cdot IR_k}{HBGV_j} \quad \text{Eq. 2}$$

where k is the exposure route (e.g. cereals (CER), Fruit and vegetable (F/V)); j is one micropollutant that may cause chronic toxicity; $C_{k,j}$ is the distribution of the concentration of the j micropollutant in the source k; IR_k is the Intake Rate (g/day) representing the daily consumption of the DW or food; $HBGV_j$ is the Health-Based Guideline Value for the j micropollutant, that is gathered from toxicological studies.

The proposed procedure includes uncertainty analyses to account for knowledge gaps, input data uncertainties and tempo-spatial variabilities, and modeling uncertainties to provide decision makers with the confidence level of the risk estimation. This is done through Monte-Carlo simulations by building the probabilistic distributions of the input variables and propagating such uncertainty distributions in the risk assessment step.

The developed procedure was applied to assess three different potential hazard sources in the IUWS:

1) Firstly, the research investigated the chronic environmental risks posed by Combined Sewer Overflows (CSOs) against wastewater treatment plant (WWTP) effluents. Worldwide literature data collection was used to build an archetype IUWS including several CSOs discharges, BP at the inlet of the WWTP, the WWTP effluent and a river as receiving surface water. These *i-th* elements (CSOs, BP, effluent, river) were characterized in terms of both water quantity (discharged volume and river flowrate) and quality (concentrations of *j-th* micropollutants), each one defined by a probability distribution, to consider data inherent uncertainty and variability. Various percentiles were extracted from these probability distributions for the parameterization of the archetype IUWS. In particular, six scenarios were identified related to climate changes: three pollution levels were accounted using the distributions for the 50th, 75th, 95th percentiles (C50, C75, C95) of the micropollutants concentration distributions; three dilution scenarios (Safe, Medium, and Worst) were derived from the distributions of the river dilution factor. This study focused on 12 micropollutants from different classes: 3 HM, 3 PHARMS, 3 PESTS, 3 PAH. Climate change scenarios have been included to predict future environmental risk trend and main drivers.

2) Additionally, an integrated model-based approach was applied to evaluate the impact of transitioning to water-wise cities on urban water quality. The assessment encompasses multiple strategies such as stormwater separation, use of Groundwater Heat Pumps (GHPs), reclaimed water for irrigation, and their implications on micropollutants release into a surface river under different scenarios. The study focused on

a city in Northern Italy, assumed as archetype city for the "water-wise city" transition, evaluating the occurrence and fate of three micropollutants: PFOA, PFOS (both in the family of PFAS) and pyrene (in the family of PAHs). Concentration data were collected from literature and open-source monitoring repositories. The fate of these micropollutants in the different water sources in the case study was predicted adopting the Integrated Urban Wastewater and Stormwater (IUWS_MP) model library in the software WEST (DHI A/S, Denmark).

3) In this context, this research critically reviewed the existing literature and proposed methodologies for assessing impacts from reclaimed wastewater reuse in agriculture. Firstly, a conceptual framework was built to evaluate the environmental compartments involved in the reclaimed wastewater reuse, the models used to assess reuse impacts and the main target variables analyzed in scientific literature focused on reuse. The study identifies gaps in existing models and proposes a unified approach to consider both environmental and human risk assessment when dealing with reclaimed wastewater reuse in agriculture.

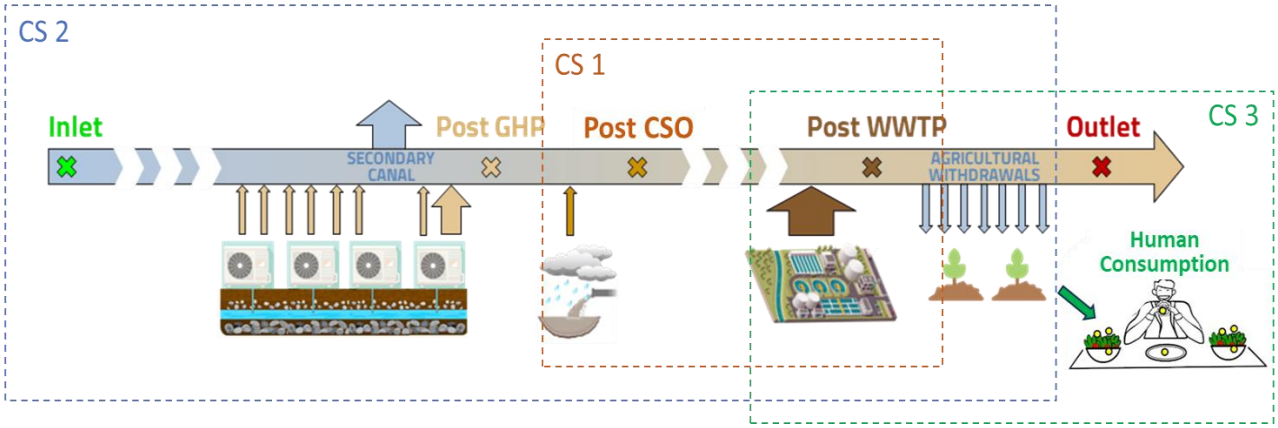

Figure 13. Schematic representation of the surface water crossing a waterwise city, with water inputs and outputs. For each Case Study (CS) the boundaries of the analyzed system are reported.

4.8.4 Results

The proposed risk-based procedure proved to be effective to identify micropollutants sources and exposure routes as useful support tool for planning monitoring campaigns.

Looking at the first task (risk derived from CSOs), comparing the risk contribution of wet-weather discharges to the normal wastewater treatment plant effluent, the RQ probabilistic distribution was used to evaluate which streams and micropollutants are more responsible for chronic environmental risk. As to micropollutants exceeding the risk threshold of RQ=1 (nRQi,j>1) in Figure 14a, the higher risk is posed by Polycyclic Aromatic Hydrocarbons (PAH), mainly present in CSOs and BP. Pharmaceuticals (PHARMS) represent the second class of concern for surface water, being the effluent the main source, while wet-weather discharges contribute to the risk only in the Worst scenario. The third class of concern is Heavy Metals (HM), with high risk in Worst scenario related to CSOs. Pesticides (PEST) pose the smallest risk to the river both in Medium and Worst scenario, with Diuron being the most critical compound.

Since in the literature there is a lack of standardization of the risk assessment procedure, this study investigated the sensitivity of the risk estimate to the risk assessment choices, such as the percentile of micropollutant's concentration used for the exposure assessment, or the different percentiles of the RQ distribution. The choice of different micropollutants concentration percentiles did not determine significant differences in the RQ values, while the choice of the dilution factor can strongly impact the risk assessment outcome. For example, for Benzo(a)Pyrene (BaP, Figure 14b) median RQ values were found to be less than 10 times higher from C50 to C95 scenario, while values are up to 10,000 times higher from Safe to Worst scenario. Therefore, an accurate risk assessment requires to correctly quantify the hydraulic variables of the IUWS (specifically the river dilution factor), as neglecting the impact of dilution and assessing only the discharged concentrations might lead to significant overestimation of the environmental risk.

(a) (b)

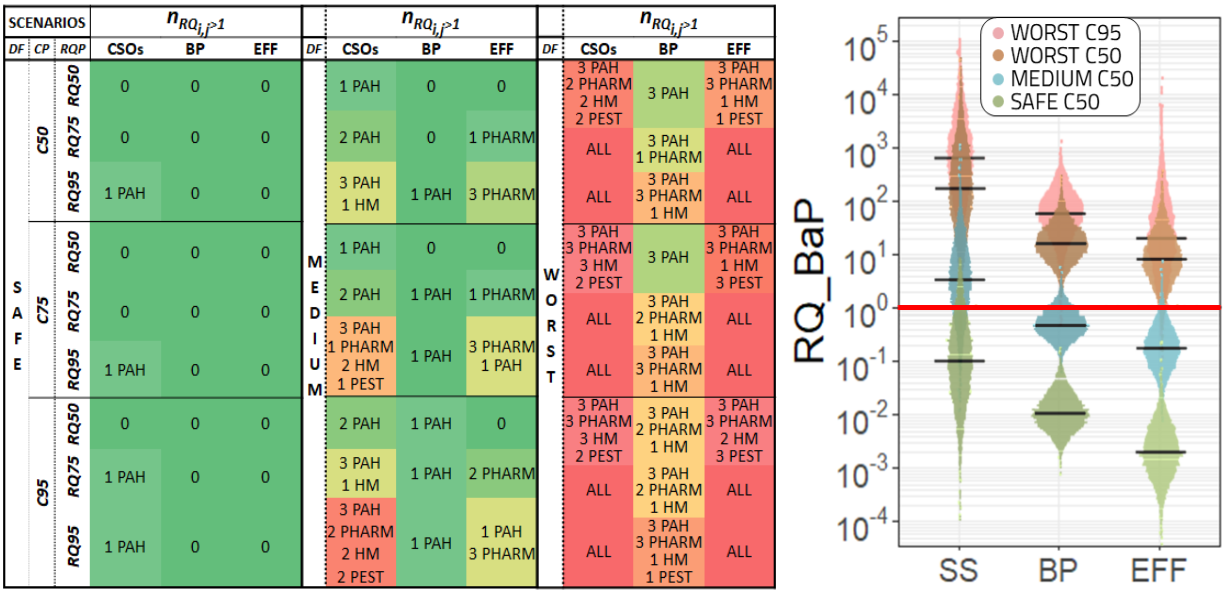

Figure 14. (a) Number of exceedances of the threshold (RQ=1) for each discharge in each scenario (DF: dilution factor scenarios, CP: pollution level scenarios), per micropollutant class. Colours from green to red represent higher nRQi,j>1. (b) RQi,j for BaP due to single discharges. (Ianes et al., 2024)

However, site-specific modeling can be needed to detect the specificity of the discharged pollution in each catchment, also based on the different nature and sources of different micropollutants. For this reason, a fate modeling tool was adopted to evaluate the specific case of the second task (impact on water quality of transitioning to water-wise cities), that faces several fluxes of water inputs and outputs. Model simulations were used to assess the environmental risk associated with the presence of the selected micropollutants in the recipient. Both chronic and acute risks were assessed in terms of Risk Quotient (RQ). The acute and chronic risks were evaluated in five monitoring points of the waterway in correspondence with different discharge points, as shown in Figure 1: (i) INLET represents the surface water upstream the city; (ii) POST_GHP is right after the discharge of the groundwater used by GHPs; (iii) POST_CSO is located right after the discharge of the separate sewer; (iv) POST_WWTP is right after the discharge of the WWTP effluent, where the withdrawals for irrigation purposes start; (v) OUTLET is at the end of the waterway.

Four scenarios were defined to understand the contribution of each source on the resulting environmental risk:

0. B (Baseline): INLET (2 m^3/s) flowing to the secondary canal (1.99 m^3/s), presence of WWTP effluent (4 m^3/s in dry-weather), agricultural withdrawals;
1. B+GHP: additional flow of water coming from the discharges of GHPs in the re-connection, with seasonal fluctuation (up to 5.8 m^3/s);
2. B+GHP+SS08: additional flow from separated sewer conveying stormwater from 8 km^2, subtracted from the WWTP catchment area;
3. B+GHP+SS24: additional flow from separated sewer conveying stormwater from 24 km^2, subtracted from the WWTP catchment area.

PFOA and PFOS did not show exceedance of the acute environmental risk threshold, showing maximum concentrations equal to 14 and 16 ng/L, respectively, throughout the year and across the various monitoring points. However, the chronic environmental risk was greater than 1 (Figure 15) also in the Baseline scenario after the discharge of the WWTP effluent. When looking at the other scenarios, a higher chronic environmental risk is present with GHP and the separated sewer, after the GHPs and SW discharges, with GHPs increasing significantly the risk.

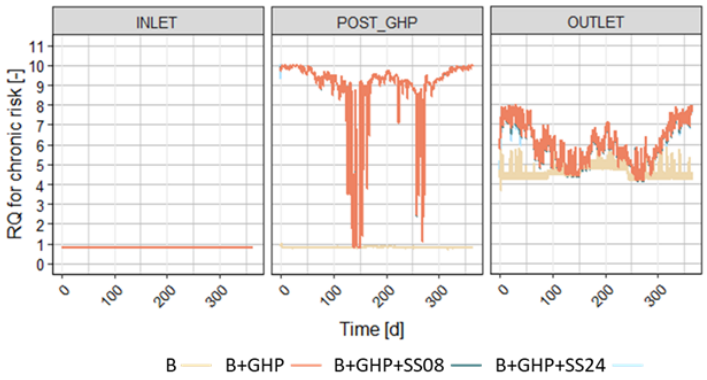

Figure 15. RQ for chronic environmental risk for the sum of PFOA and PFOS in PFOA equivalents, in different monitoring points for the four analyzed scenarios.

The main contribution of PFAS is given by the WWTP effluent in the Baseline scenario, especially in the wet-weather days. When GHPs are considered, their contribution determines a higher concentration in the waterway and hence a higher risk, which is lowered by the dilution effect by the WWTP effluent. The strong variability in the locations POST_GHP refers to the period when GHP are less/not in use (spring and fall). When GHPs are not in use, the risk lowers down to an acceptable level (RQ<1). Differently from PFAS, which can be considered ubiquitous micropollutants, the main source of pyrene was found to be urban water runoff. As to the acute risk, no exceedances are shown in the B and B+GHP scenarios, and no exceedances are present at the INLET and POST_GHP monitoring points in all scenarios. Instead, RQ higher than the threshold of 1 are found for pyrene in surface water during wet weather only at the locations POST_SW and POST_WWTP, where stormwater is discharged, and at the OUTLET. Thus, the combination of literature concentration data collection, advanced modeling and risk assessment was proved to be effective in identifying the main sources of contamination in urban areas for different micropollutants.

Finally, in the third task, a focus was pointed on the reuse of reclaimed wastewater in agriculture as another potential source of risk for both the environment, where the reclaimed wastewater is released, and human health, due to the consumption of irrigated crops. A literature review was conducted to evaluate what are the main modeled impacts of wastewater reuse and what are the current gaps to be filled to have a proper evaluation of such practice. The Scopus database was used for collecting studies written in English and published in the period 2017-2023 from peer-reviewed journals related to wastewater reuse in agriculture, leading to 163 articles. Each study was classified based on three analyzed features:

a) The environmental compartments addressed: (i) WWTP, (ii) environment (intended as the surface water receiving the WWTP effluent), (iii) irrigation system, (iv) soil, (v) crop and (vi) humans.

b) The applied impact models divided into "quantity-based" impact models: (i) water mass flow analysis, (ii) Life Cycle Assessment (LCA), (iii) cost analysis, (iv) energy consumption estimation, and (v) social analysis; and "quality-based" impact models: (vi) treatment processes, (vii) effects on soil, (viii) effects on crop, (ix) environmental risk and (x) human risk.

c) The modelled variables: (i) water volume for the quantity-based impact models, and (ii) microbial, (iii) ARBs (iv) CECs, (v) heavy metals, (vi) nutrients, (vii) salinity and (viii) conventional contaminants (i.e., organic matter and suspended solids) for the quality-based impact models.

It was highlighted that the main literature gap related to reclaimed wastewater reuse is due to the lack of studies applying both environmental and human risk assessment. In particular, there are only a few studies evaluating these effects and there are no research works focusing on the combination of environmental and human health risk assessments to jointly evaluate these risks in a One-Health perspective. Thus, literature results on the human health risk due to the presence of four micropollutants in irrigated crops were used to simultaneously calculate the environmental risk due to the concentration of these micropollutants in the surface water used for irrigation (Figure 16).

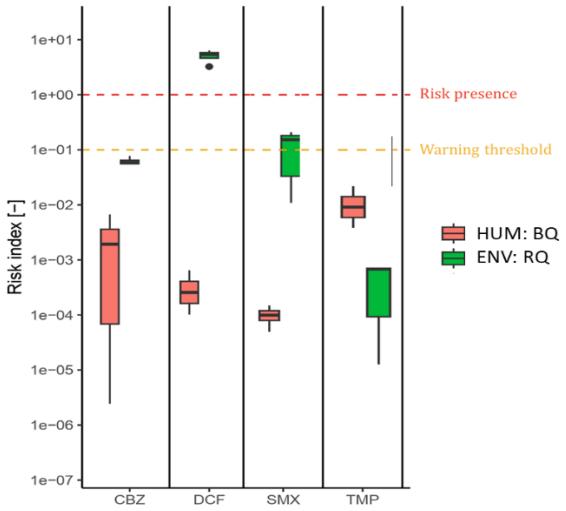

Figure 16. Estimated risk indices distributions in terms of human health and environmental risk, differentiated for the analyzed micropollutants: carbamazepine (CBZ), diclofenac (DCF), sulfamethoxazole (SMX) and trimethoprim (TMP). Dashed lines indicate risk indices values equal to the thresholds of 0.1 and 1.

The human health risk related to the indirect reuse of reclaimed wastewater is substantially lower than the warning threshold (BQ equal to 0.1) for all the considered micropollutants. Thus, it can be stated that the presence of these contaminants in the reclaimed wastewater used (diluted by the natural surface water stream) for crop irrigation does not pose a risk to human health. However, the environmental risk gives a significant contribution to the overall risk, being always statistically higher than the human health risk, except for trimethoprim, Thus, for these micropollutants an increased attention would be recommendable, in terms of regulatory measures or additional targeted monitoring campaigns. This analysis underscores the importance of a holistic risk assessment employing a ONE-Health approach, which, rather than limiting the risk evaluation to a singular endpoint, it should evaluate the different ones for each micropollutant to determine their contribution to the overall risk and identify the most critical endpoint useful to prioritize regulations and monitoring.

4.8.5 Scientific products and dissemination

Published Papers:

Ianes, J., Cantoni, B., Remigi, E. U., Polesel, F., Vezzaro, L., & Antonelli, M. (2023). A stochastic approach for assessing the chronic environmental risk generated by wet-weather events from integrated urban wastewater systems. Environmental Science: Water Research & Technology, 9(12), 3174-3190.

Presentations at conferences:

Penserini, L., Cantoni, B., & Antonelli, M. (2023). Reclaimed wastewater reuse impacts: from literature data gaps to integrated risk modelling. 6th IWA International Conference on eco-Technologies for Wastewater Treatment (ecoSTP2023), Girona (Spain), 26-29 June 2023.

Ianes, J., Cantoni, B., Remigi, E. U., Polesel, F., Vezzaro, L., & Antonelli, M. (2023). Assessing the contribution of wet-weather discharges on micropollutants release by urban catchments. 11th IWA International Conference on Efficient Urban Water Managment “Efficient2023”, Bordeaux (France), 13-15 September 2023.

Ianes, J., Cantoni, B., Scana, F., Delli Compagni, R., Remigi, E. U., Polesel, F., Vezzaro, L., & Antonelli, M. (2023). An integrated modelling framework to assess cascade water reuse in urban areas. 11th IWA International Conference on Efficient Urban Water Managment “Efficient2023”, Bordeaux (France), 13-15 September 2023.

5 Conclusions

The approaches, methodologies and modelling tools developed and implemented in T4.3.1 during the first 15 months of the project have set up a thorough framework for the identification, assessment, categorization and quantification of environmental risks associated to the presence of contaminants of different nature in various environmental compartments including terrestrial water ecosystems, groundwater and soils.

Two of the envisaged milestones of the project have been reached at this stage of the activities, namely:

- M4.1 - Detailed plan of the technical-scientific basics (expected at month 1): all the participants to the task have conducted a thorough review of the existing technical and scientific background in their respective fields of investigation, and most of the retrieved data and related findings/implications have been published in the form of scientific papers or included in data repositories or databases (see sections 4.1.5, 4.2.4, 4.3.5, 4.4.7, 4.6.4, 4.7.5 and 4.8.5 for further details)
- M4.2 - Monitoring and data collection (expected at month 12): as outlined in the abstract and further detailed in the individual technical sections, monitoring of environmental data through both conventional and innovative techniques, collection of environmental data along with their classification and systematization, as well as processing and interpretation are core actions of all the activities conducted. While large datasets have been collected so far and have been already used for environmental modelling and assessment, the interpretation of the results of the investigation may also indicate the need for further implementation of the collected data. This will be the subject of future activities in order to refine the model accuracy, improve the reliability of the results, reduce the degree of the uncertainty and ensure preservation of the complexity of environmental processes and phenomena.

In summary, the relevant results/findings and the main related products of the activities conducted so far include (referring to the three thematic areas mentioned in the Abstract):

1. **Development, application and validation of methods and protocols for the detection and quantification of contaminants in the environment:**
   i. development of protocols and analytical techniques (LDIR, HSI) to characterize the transformations of residual bioplastics in waste treatment processes and the identification of microplastics and micro-bioplastics in solid (waste, sludge, soil) and liquid (groundwater, wastewater) matrices (UNIFI, UNIROMA1);
   ii. quantified biodurability and activity of hazardous (asbestos, erionite) and potentially hazardous (antigorite) mineral fibres in biological fluids of humans (UNIROMA1).
2. **Development, application and validation of methods for advanced environmental monitoring:**
   i. gained evidence of microplastics contamination in three Italian groundwater bodies (UNIFI);
   ii. production of a hydrogeological geo-database summarising all the information collected in the Volturno Plain in the last two decades in a usable and interactive format (UNINA);
   iii. design of a platform to evaluate absolute nanoscale topographic data of minerals subject to reaction (POLIMI);
   iv. development of integrated models to support the transition to water-wise cities, addressing micropollutant impacts (POLIMI);
   v. selection of methods and equipment for monitoring of emitted fluxes of hydrocarbon vapours from the subsurface soil of petroleum-contaminated sites (UNIPA).
3. **Data analysis and modelling of transport, diffusion, transformation, degradation of contaminants as well as prediction of their effects on human health, flora, fauna and environment quality:**
   i. gained evidence of risks caused by microplastics on plants, crops and stygofauna (UNIFI);
   ii. analytical approximations of model parameters built to describe the early and late time behaviour of solute breakthrough curves in surface water (UNIPD);
   iii. limit condition derived for parameter identification of longitudinal dispersion and first-order mass transfer in storage zones of surface water (UNIPD);
   iv. use of collected literature data, models and risk assessment tools to identify micropollutants sources, fate and generated risk for combined sewer overflows and wastewater reuse systems (POLIMI);

v. use of statistical methods, sensitivity analysis and uncertainty estimation for improved analysis of environmental data (UNINA, POLIMI).

6 References

6.1.1 References for chapter 4.2

Amigo, J. M., Martí, I., & Gowen, A. (2013). Hyperspectral imaging and chemometrics: A perfect combination for the analysis of food structure, composition and quality. In Data handling in science and technology (Vol. 28, pp. 343-370). Elsevier.

Ballabio, D., & Consonni, V. (2013). Classification tools in chemistry. Part 1: linear models. PLS-DA. Analytical methods, 5(16), 3790-3798.

Bracciale, M.P., De Gioannis, G., Falzarano, M., Muntoni, A., Polettini, A., Pomi, R., Rossi, A., Sarasini, F., Tirillò, J., Zonfa, T., 2024. Disposable Mater-Bi® bioplastic tableware: Characterization and assessment of anaerobic biodegradability. Fuel 355, 129361. https://doi.org/10.1016/J.FUEL.2023.129361

Buswell, A.M., Mueller, H.F., 1952. Mechanism of Methane Fermentation. Ind. Eng. Chem. 44, 550–552. https://doi.org/10.1021/ie50507a033

Calabrò, P.S., Grosso, M., 2018. Bioplastics and waste management. Waste Manag. https://doi.org/10.1016/j.wasman.2018.06.054

Cazaudehore, G., Guyoneaud, R., Evon, P., Martin-Closas, L., Pelacho, A.M., Raynaud, C., Monlau, F., 2022. Can anaerobic digestion be a suitable end-of-life scenario for biodegradable plastics? A critical review of the current situation, hurdles, and challenges. Biotechnol. Adv. 56, 107916. https://doi.org/https://doi.org/10.1016/j.biotechadv.2022.107916

Falzarano, M., Polettini, A., Pomi, R., Rossi, A., Zonfa, T., 2023. Anaerobic Biodegradability of Commercial Bioplastic Products: Systematic Bibliographic Analysis and Critical Assessment of the Latest Advances. Materials (Basel). 16. https://doi.org/10.3390/ma16062216

Rinnan, Å., Van Den Berg, F., & Engelsen, S. B. (2009). Review of the most common pre-processing techniques for near-infrared spectra. TrAC Trends in Analytical Chemistry, 28(10), 1201-1222.

6.1.2 References for chapter 4.4

Allocca V, Celico F, Celico P, De Vita P, Fabbrocino S, Mattia C, Musilli I, Piscopo V, Summa G (2005) Hydrogeological Map of Southern Italy. Istituto Poligrafico e Zecca dello Stato, Roma Corniello A,

Corniello A, Ducci D (2014) Hydrogeochemical characterization of the main aquifer of the "Litorale Domizio-Agro Aversano NIPS" (Campania — southern Italy). Journal of Geochemical Exploration, 137:1-10, https://doi.org/10.1016/j.gexplo.2013.10.016

DAM (Autorità di Bacino Distrettuale dell'Appennino Meridionale) (2021). Piano di Gestione delle Acque Ciclo 2021–2027. Available online: https://www.distrettoappenninomeridionale.it/index.php/piano-iii-fase-2021-2027-menu/piano-di-gestione-acqueiii-ciclo-2021-2027-menu

Ducci D, Della Morte R, Mottola A, Onorati G, Pugliano G (2020) Evaluating upward trends in groundwater nitrate concentrations: an example in an alluvial plain of the Campania region (Southern Italy). Environmental Earth Sciences 79:319, https://doi.org/10.1007/s12665-020-09062-8

Sellerino M, Corniello A, Ducci D (2016) Investigation of Groundwater Systems at different scale: the case study of the Volturno River Plain (Campania, Italy). Rendiconti Online della Società Geologica Italiana, 41:76-79, https://doi.org/10.3301/ROL.2016.97

6.1.3 References for chapter 4.6

Appelo, C. A. J., & Postma, D. (2005). Geochemistry, groundwater and pollution: Leiden, The Netherlands.

Arvidson, R. S., Ertan, I. E., Amonette, J. E., & Luttge, A. (2003). Variation in calcite dissolution rates: A fundamental problem?. Geochimica et cosmochimica acta, 67(9), 1623-1634.

Barri, C., Mafakheri, E., Fagiani, L., Tavani, G., Barzaghi, A., Chrastina, D., ... & Bollani, M. (2020). Engineering of the spin on dopant process on silicon on insulator substrate. Nanotechnology, 32(2), 025303.

Bibi, I., Arvidson, R. S., Fischer, C., & Lüttge, A. (2018). Temporal evolution of calcite surface dissolution kinetics. Minerals, 8(6), 256.

Bollermann, T., & Fischer, C. (2020). Temporal evolution of dissolution kinetics of polycrystalline calcite. American Journal of Science, 320(1), 53-71.

Bouissonnié, A., Daval, D., Marinoni, M., & Ackerer, P. (2018). From mixed flow reactor to column experiments and modeling: Upscaling of calcite dissolution rate. Chemical Geology, 487, 63-75.

Brand, A. S., Feng, P., & Bullard, J. W. (2017). Calcite dissolution rate spectra measured by in situ digital holographic microscopy. Geochimica et cosmochimica acta, 213, 317-329.

Carrera, J., & Neuman, S. P. (1986). Estimation of aquifer parameters under transient and steady state conditions: 1. Maximum likelihood method incorporating prior information. Water Resources Research, 22(2), 199-210.

Ceresa, L., Guadagnini, A., Rodríguez-Escales, P., Riva, M., Sanchez-Vila, X., & Porta, G. M. (2023). On Multi-Model Assessment of Complex Degradation Paths: The Fate of Diclofenac and Its Transformation Products. Water Resources Research, 59(1), e2022WR033183.

Dell'Oca, A., Riva, M., & Guadagnini, A. (2017). Moment-based metrics for global sensitivity analysis of hydrological systems. Hydrology and Earth System Sciences, 21(12), 6219-6234.

Dell'Oca, A., Guadagnini, A., & Riva, M. (2023). Probabilistic assessment of failure of infiltration structures under model and parametric uncertainty. Journal of environmental management, 344, 118466.

Doherty, J. (2015). Calibration and uncertainty analysis for complex environmental models (p. 227pp). Brisbane, Australia: Watermark Numerical Computing

Duda, R. O. (2001). Hart PE, Stork DG. Pattern Classification. New York: Wiley.

Dulio, V., & Slobodnik, J. (2009). NORMAN—network of reference laboratories, research centres and related organisations for monitoring of emerging substances. Environmental Science and Pollution Research, 16, 132-135.

Emmanuel, S. (2014). Mechanisms influencing micron and nanometer-scale reaction rate patterns during dolostone dissolution. Chemical Geology, 363, 262-269.

Fischer, C., Arvidson, R. S., & Lüttge, A. (2012). How predictable are dissolution rates of crystalline material?. Geochimica et Cosmochimica Acta, 98, 177-185.

Fischer, C., & Luttge, A. (2018). Pulsating dissolution of crystalline matter. Proceedings of the National Academy of Sciences, 115(5), 897-902.

Guren, M. G., Putnis, C. V., Montes-Hernandez, G., King, H. E., & Renard, F. (2020). Direct imaging of coupled dissolution-precipitation and growth processes on calcite exposed to chromium-rich fluids. Chemical Geology, 552, 119770.

Harstad, A. O., & Stipp, S. L. S. (2007). Calcite dissolution: Effects of trace cations naturally present in Iceland spar calcites. Geochimica et Cosmochimica Acta, 71(1), 56-70.

Heberling, F., Bosbach, D., Eckhardt, J. D., Fischer, U., Glowacky, J., Haist, M., ... & Winkler, B. (2014). Reactivity of the calcite–water-interface, from molecular scale processes to geochemical engineering. Applied geochemistry, 45, 158-190.

James, G., Witten, D., Hastie, T., & Tibshirani, R. (2013). An introduction to statistical learning (Vol. 112, p. 18). New York: springer.

Julia, M., Putnis, C. V., King, H. E., & Renard, F. (2023). Coupled dissolution-precipitation and growth processes on calcite, aragonite, and Carrara marble exposed to cadmium-rich aqueous solutions. Chemical Geology, 621, 121364.

Lasaga, A. C., & Lüttge, A. (2001). Variation of crystal dissolution rate based on a dissolution stepwave model. Science, 291(5512), 2400-2404.

Lasaga, A. C., & Lüttge, A. (2003). A model for crystal dissolution. European Journal of Mineralogy, 15(4), 603-615.

Lüttge, A., Arvidson, R. S., & Fischer, C. (2013). A stochastic treatment of crystal dissolution kinetics. Elements, 9(3), 183-188.

Marinello, F., Carmignato, S., Voltan, A., Savio, E., & De Chiffre, L. (2010). Error sources in atomic force microscopy for dimensional measurements: Taxonomy and modeling.

Noiriel, C., Oursin, M., Saldi, G., & Haberthür, D. (2018). Direct determination of dissolution rates at crystal surfaces using 3D X-ray microtomography. ACS Earth and Space Chemistry, 3(1), 100-108.

Parkhurst, D. L., & Appelo, C. A. J. (2013). Description of input and examples for PHREEQC version 3—a computer program for speciation, batch-reaction, one-dimensional transport, and inverse geochemical calculations. US geological survey techniques and methods, 6(A43), 497.

Recalcati, C., Siena, M., Riva, M., & Guadagnini, A. (2023). Experimental assessment of calcite dissolution patterns through Atomic Force Microscopy. Reference Module in Chemistry, Molecular Sciences and Chemical Engineering, Elsevier

Renard, F., Putnis, C. V., Montes-Hernandez, G., King, H. E., Breedveld, G. D., & Okkenhaug, G. (2018). Sequestration of antimony on calcite observed by time-resolved nanoscale imaging. Environmental science & technology, 52(1), 107-113.

Renard, F., Røyne, A., & Putnis, C. V. (2019). Timescales of interface-coupled dissolution-precipitation reactions on carbonates. Geoscience Frontiers, 10(1), 17-27.

Ricci, D., & Braga, P. C. (2004). Recognizing and avoiding artifacts in AFM imaging. Atomic Force Microscopy: Biomedical Methods and Applications, 25-37.

Siena, M., Bussetti, G., Recalcati, C., Riva, M., Duò, L., & Guadagnini, A. (2021). Statistical characterization of heterogeneous dissolution rates of calcite from in situ and real-time AFM imaging. Transport in Porous Media, 140, 291-312.

Siena, M., Recalcati, C., Guadagnini, A., & Riva, M. (2023). A Gaussian-Mixture based stochastic framework for the interpretation of spatial heterogeneity in multimodal fields. Journal of Hydrology, 617, 128849.

Silver, M., Kübeck, C., Wefer-Roehl, A., & Schüth, C., (2016). Column Experiments Results - MAR Column Experiments with Soils from MARSOL Demonstration Sites in Greece and Israel. Deliverable D14.3 of MARSOL (Demonstrating Managed Aquifer Recharge as a Solution to Water Scarcity and Drought) project, funded by the European Union's Seventh Framework Programme for Research, Technological Development and Demonstration under grant agreement 619120.

Silver, M., Selke, S., Balsaa, P., Wefer-Roehl, A., Kübeck, C., & Schüth, C. (2018). Fate of five pharmaceuticals under different infiltration conditions for managed aquifer recharge. Science of the total environment, 642, 914-924.

Teng, H. H. (2004). Controls by saturation state on etch pit formation during calcite dissolution. Geochimica et Cosmochimica Acta, 68(2), 253-262.

6.1.4 References for chapter 4.5

ASTM (2000), Standard Guide for Risk-Based Corrective Action, Designation: E-2081-00.

Cotel, S., Schäfer, G., Traverse, S., Marzougui-Jaafar, S., Gay, G., Razakarisoa, O., 2015. Evaluation of VOC fluxes at the soil-air interface using different flux chambers and a quasi-analytical approach. Water Air Soil Pollut. 226 (11), 356.

Eklund, B., 1992. Practical guidance for flux chamber measurements of fugitive volatile organic emission rates. J. Air Waste Manag. 42 (12), 1583–1591.

Gao, F., Yates, S.R., 1998. Laboratory study of closed and dynamic flux chambers: experimental results and implications for field application. J. Geophys. Res.-Atmos. 103 (D20), 26115–26125.

Gidudu, B., Chirwa, E. M. N. (2020). Biosurfactants as demulsification enhancers in bio-electrokinetic remediation of petroleum contaminated soil. Proc. Saf. Environ. Prot., 143, 332–339. https://doi.org/10.1016/j.psep.2020.05.052.

Heinemeyer, A., McNamara, N.P., 2011. Comparing the closed static versus the closed dynamic chamber flux methodology: implications for soil respiration studies. Plant Soil 346 (1–2), 145–151

Hudson, N., Ayoko, G.A., 2008. Odour sampling. 2. Comparison of physical and aerodynamic characteristics of sampling devices: a review. Bioresour. Technol. 99 (10), 3993–4007.

Islam, M.N., Jung, S.K., Jung, H.-Y., Park, J.-H. (2017). The feasibility of recovering oil from contaminated soil at petroleum oil spill site using a subcritical water extraction technology. Proc. Saf. Env. Prot. 111, 52-59. http://dx.doi.org/10.1016/j.psep.2017.06.015

Labianca, C., De Gisi, S., Pannarale, G., Specchio, V., Notarnicola, M. (2019). Confronto tra differenti versioni del software risk-net per la valutazione del rischio sanitarioambientale di un sito contaminato di interesse nazionale. Ingegneria dell'ambiente, 6(3), 175- 182. dx.doi.org/10.32024/ida.v6i3.223 (in Italian).

Legislative Decree N: 152/2006. Norme in materia ambientale (G.U. n. 88 14 aprile 2006) (in Italian).

Pihlatie, M.K., Christiansen, J.R., Aaltonen, H., Korhonen, J.F., Nordbo, A., Rasilo, et al., 2013. Comparison of static chambers to measure CH 4 emissions from soils. Agric. For. Meteorol. 171, 124–136

Saponaro, S., Sezenna, E., Careghini, A., Mastorgio, A., Spinelli, L. (2016). Open Dynamic Flux Chamber. Patent No. WO/2016/067166.

SNPA, (2018a). Progettazione del monitoraggio dei vapori nei siti contaminati. Linea Guida SNPA 15/2018 (in Italian).

SNPA, (2018b). Metodiche analitiche per le misure di aeriformi nei siti contaminati. Linea Guida SNPA 16/2018 (in Italian).

SNPA, (2018c). Procedura operativa per la valutazione e l'utilizzo dei dati derivanti da misure di gas interstiziali nell'analisi di rischio dei siti contaminati. Linea Guida SNPA 17/2018 (in Italian).

U.S.EPA, 1986. Measurement of gaseous emission rates from land surfaces using an emission isolation flux chamber: user's guide. EPA/600/8-86/008.

Verginelli, I., Pecoraro, R., Baciocchi, R. (2018). Using dynamic flux chambers to estimate the natural attenuation rates in the subsurface at petroleum contaminated sites. Science of the Total Environment 619–620, 470–479. https://doi.org/10.1016/j.scitotenv.2017.11.100.

6.1.5 References for chapter 4.7

Abramowitz, M., & I. A. Stegun, (1972), Handbook of mathematical functions, National Bureau of Standards Applied Mathematics Series - 55.

Bencala, K., & R. A. Walters, (1983), Simulation of solute transport in a mountain pool-and-riffle stream - A transient storage model, Water Resources Research, 19(3), 718-724, doi:10.1029/WR019i003p00718.

Bottacin-Busolin, A., A. Marion, T. Musner, M. Tregnaghi, & M. Zaramella (2011), Evidence of distinct contaminant transport patterns in rivers using tracer tests and a multiple domain retention model, Advances in Water Resources, 34(6), 737–746, doi:10.1016/j.advwatres.2011.03.005.

Briggs, M. A., M. N. Gooseff, C. D. Arp, & M. A. Baker (2009), A method for estimating surface transient storage pa-rameters for streams with concurrent hyporheic storage, Water Resour. Res., 45(4), W00D27, doi:10.1029/2008WR006959.

Chatwin, P. C., (1971). On the interpretation of some longitudinal dispersion experiments, J. Fluid Mech., 1971, 48, 689–702.

Davis, P. M., & T. C. Atkinson (2000), Longitudinal dispersion in natural channels: 3. An aggregated dead zone model applied to the River Severn, Hydrol. Earth Syst. Sci., 4(3), 373–381, doi10.5194/hess-4-373-2000.

Marion, A., M. Zaramella, M., & A. I. Packman, A. (2003), Parameter Estimation of the Transient Storage Model for Stream–Subsurface Exchange, J. Environ. Eng., 129(5), 456–463, doi:10.1061/(ASCE)0733-9372(2003)129:5(456).

Marion, A., & M. Zaramella, (2005), Diffusive behavior of bedform-induced hyporheic exchange in rivers, Journal of Environmental Engineering, 131(9), 1260–1266, doi:10.1061/(ASCE)0733-9372(2005)131:9(1260).

Marion, A., M. Zaramella, and A. Bottacin-Busolin (2008), Solute transport in rivers with multiple storage zones: The STIR model, Water Resour. Res., 44, W10406, doi:10.1029/2008WR007037.

Mulholland, P. J., E. R. Marzolf, J. R. Webster, D. R. Hart, & S. P. Hendricks (1997), Evidence of hyporheic retention of phosphorus in Walker Branch, Limnol. Oceanogr., 42, 443–451.

Valett, H. M., J. A. Morrice, & C. N. Dahm (1996), Parent lithology, surface-groundwater exchange, and nitrate retention in headwater streams, Limnol. Oceanogr., 41, 333–345.

Zaramella, M., A. I. Packman, & A. Marion (2003), Application of the transient storage model to analyze advective hyporheic exchange with deep and shallow sediment beds, Water Resour. Res., 39(7), 1198, doi:10.1029/2002WR001344.